Sang-Ho Lee
Samuel Krimm
*Biophysics Research Division
and Department of Physics,
The University of Michigan,
Ann Arbor, Michigan 48109*

Ab Initio-Based Vibrational Analysis of α-Poly(L-alanine)

Abstract: *Polarized ir and Raman spectra have been obtained on oriented films of α-helical poly(L-alanine) (α-PLA) and its N-deuterated derivative. These improved spectra permit a more complete assignment of observed bands to A-, E_1-, and E_2-species modes. A new empirical force field has been refined, based on ab initio force fields of N-methylacetamide and L-alanyl-L-alanine, which reproduces observed frequencies above 200 cm^{-1} to less than 5 cm^{-1}. A new transition dipole coupling treatment avoids the weak coupling and perturbation approximations, and can now account for the newly observed and reassigned amide I (E_2) mode. As a result of this improved force field, several other observed bands have also been reassigned.* © 1998 John Wiley & Sons, Inc. Biopoly 46: 283–317, 1998*

INTRODUCTION

Poly(L-alanine) (PLA) is the simplest L-type polypeptide, with a methyl group as its side chain. Much attention has been paid to this molecule as a first step in understanding the structures and properties of polypeptides and proteins. It is well known that this molecule can take on a (folded) right-handed α-helix or an (extended) antiparallel-chain pleated β-sheet conformation, depending on the sample preparation methods. There have been extensive studies of the ir[1–8] and Raman[9–15] spectra of α-PLA, and several normal mode calculations on α-PLA, based on empirical force fields, have also been done.[3,7,8,16–18] While such analyses have enhanced our basic understanding of the vibrational dynamics of helical polypeptide chain structures,[19] their accu-racy is still amenable to significant improvement, through better data and improved force fields.

Vibrational normal modes of an infinite regular helix, in this case assumed to be an α-helix, are characterized by A, E_1, and E_2 symmetry species, where A and E_1 modes are ir active, and A, E_1, and E_2 modes are Raman active.[20,21] For a complete vibrational analysis of α-PLA, it is essential to experimentally separate and assign all the modes belonging to each symmetry species. Separation of A and E_1 modes is usually possible through the use of polarized ir radiation with an oriented sample, and such extensive work on α-PLA was done by Elliott.[1] Fanconi et al.[10] obtained the explicit forms of Raman tensors corresponding to the three symmetry species, and partially succeeded in separating modes of each symmetry species for α-PLA by us-

ing polarized laser radiation. We have now been able to get improved polarized Raman spectra of uniaxially oriented samples of α-PLA and its N-deuterated analogue, α-PLA-ND, and have been able to clearly separate most modes belonging to each symmetry species.[22] Polarized ir and far-ir spectra were also measured on such samples and its N-deuterated analogue.

Although the previous normal mode analyses from our laboratory[8,18] provided a deeper understanding of the vibrational spectra of α-PLA, they were only partially testable in the sense that no polarized ir spectrum for the N-deuterated analogue of α-PLA was available and the separation of Raman E_2 modes from A and E_1 modes was not complete at that time. Our polarized Raman spectra of α-PLA-ND[22] have now also enabled us to correct earlier results: thus the previously reported 1158 cm^{-1} Raman band[13,18] turns out to be a misreading for the correct band at 1134 cm^{-1}.[22] Our new polarized ir spectra of α-PLA have also enabled us to identify a band at 639 cm^{-1}, which was unnoticed in previous experiments, and to assign it to the amide V A-species mode.

Based on these new experimental results, we have done a more rigorous normal mode analysis for α-PLA (more explicitly α_I-PLA[18]). In order to give a more physical meaning to the refined peptide force field in this calculation, the initial force constants were based on ab initio peptide force fields for various conformers of *trans*-N-methylacetamide (NMA) and L-alanyl-L-alanine [(L-Ala)$_2$].[23,*] Recent developments in computational physics enable quantum mechanical ab initio calculations to provide nearly complete properties of small molecules, such as minimum energy structures, force constants, and vibrational intensities. In an effort to find a more reliable force field applicable to polypeptides and proteins, several detailed ab initio quantum mechanical calculations have been initiated from our laboratory for small peptides like NMA[24,25] and (L-Ala)$_2$.[26–28] We have utilized these results to provide a more complete and reasonable starting set for the force field optimization. While previ-

ous empirical peptide force fields are reasonably applicable to vibrational analyses of polypeptide systems,[19] it is important to develop an improved empirical force field for α-PLA based on ab initio calculations and our new experimental data, since the quantum mechanical results give a much better representation of the real interactions in the molecule.

EXPERIMENTAL

The PLA samples used in this study were purchased from Sigma Chemical Co. (molecular weight based on viscosity determination $\approx 23,000$). The experimental details for N-deuteration of the PLA chain and for the preparation of uniaxially oriented samples are given elsewhere.[22] For the ir spectra in the 4000–500 cm^{-1} region, oriented films were made on a AgCl plate. For the far-ir spectra in the 600–50 cm^{-1} region and for the Raman spectra, oriented samples were made on a glass slide and sample films were separated later from the glass. The residual solvent dichloroacetic acid (DCA) was removed from the film by extraction with diethyl ether or pure water followed by drying in a vacuum oven at 40°C. During the extraction, the sample film for far-ir and Raman spectra usually separated by itself from the glass slide. The separated sample film was used directly for far-ir while it was mounted again on a glass slide for Raman spectra.

The detailed procedures to measure polarized Raman shifts and the resulting Raman spectra for α-PLA are given elsewhere.[22] Under our experimental setup the observed polarized A, E_1, and E_2 spectra correspond to the polarizability tensor components α_{zz}, α_{xz}, and α_{xy}, respectively, where the sample orientation direction is chosen as the z-axis. It should be noted that in the case of a uniaxially oriented sample, i.e., with random orientation about the helix axis, one cannot independently separate Raman bands due to the polarizability component α_{xx} (A species) from those due to α_{xy} (E_2 species), and our polarized E_2 spectrum will also contain A-species bands from α_{xx}.[22] However, a band in the E_2 spectrum can be confidently assigned to the E_2 species if its frequency value is significantly different from that of the corresponding band in the A (α_{zz}) and E_1 spectra, while it might be due to α_{xx} (A species) if it has nearly the same frequency as the corresponding band in the A spectrum.[22]

Infrared spectra of α-PLA were obtained on a Bomem DA-3 Fourier transform ir spectrometer at 2 cm^{-1} resolution, and are shown in Figure 1. In recording the ordinary range polarized ir spectra, a KRS-5 polarizer was mounted between the MCT detector (operating at liquid nitrogen temperature) and the KBr beam splitter, with a typical number of scans being 200. For far-ir spectral measurements, mylar films with different thicknesses were used as beam splitters together with a DTGS pyroelectric detector (operating at room temperature), and a

---

* During the preparation of this paper we noticed that the refined force field in Ref. 23 contains one erroneous force constant: instead of $f(\mathrm{NH_s}, \mathrm{CO\ s\ 3^*})$, which is considered to be important, the interaction force constant $f(\mathrm{C_\alpha C\ s}, \mathrm{CO\ 3^*})$, which is small enough to be neglected, was mistakenly used in the input. The present newly refined force field has corrected this error, and although some force constants are different from the previous ones, there are only slight changes in the physical descriptions of a small number of normal modes.
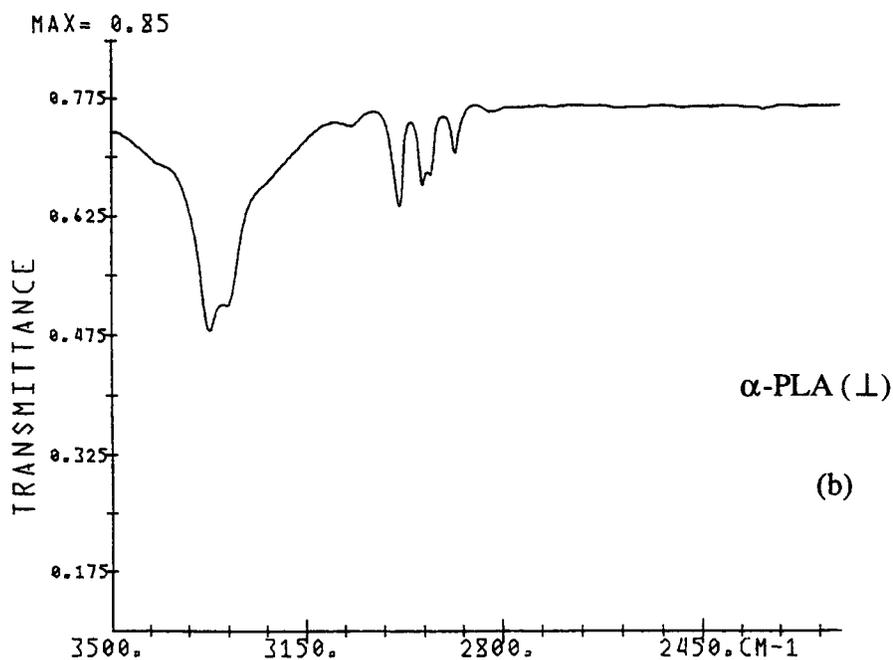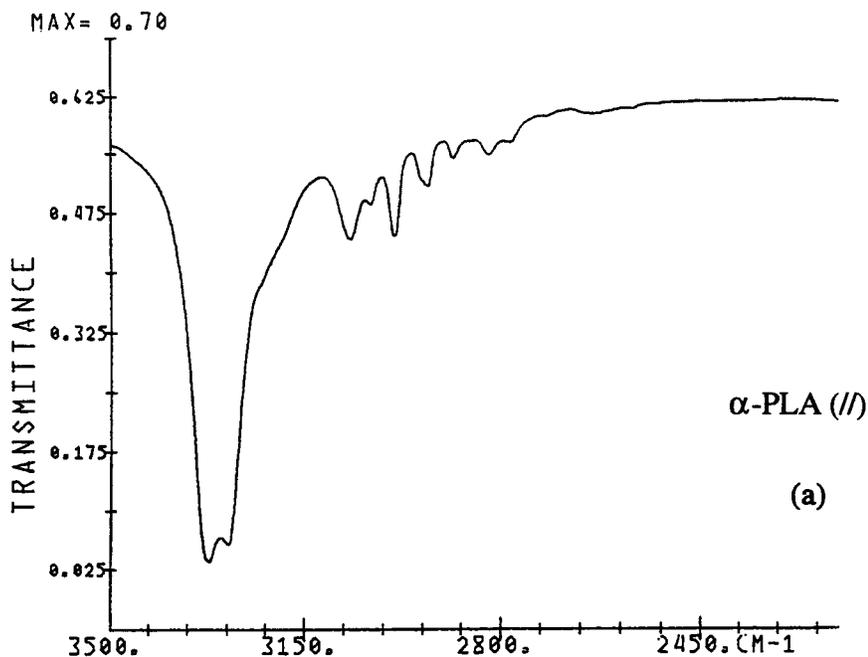
FIGURE 1 Polarized ir and far-ir spectra of α-PLA and its N-deuterated analogue. ‖: Electric vector of radiation is parallel to the sample orientation direction and ⊥: electric vector of radiation is perpendicular to the sample orientation direction. The 2200–3500 cm^{-1} region: (a) α-PLA (‖); (b) α-PLA (⊥); (c) α-PLA-ND (‖); (d) α-PLA-ND (⊥). The 500–1700 cm^{-1} region: (e) α-PLA (‖); (f) α-PLA (⊥); (g) α-PLA-ND (‖); (h) α-PLA-ND (⊥). The 200–700 cm^{-1} region: (i) α-PLA (‖); (j) α-PLA (⊥); (k) α-PLA-ND (‖); (l) α-PLA-ND (⊥). The 25–230 cm^{-1} region: (m) and (o) α-PLA (‖); (n) and (p) α-PLA (⊥); (q) and (s) α-PLA-ND (‖); (r) and (t) α-PLA-ND (⊥).

MAX= 0.90

α-PLA-ND (//) (c)

TRANSMITTANCE

0.850
0.750
0.650
0.550
0.450

3500. 3150. 2800. 2450.CM⁻¹

MAX= 0.90

α-PLA-ND (⊥) (d)

TRANSMITTANCE

0.850
0.750
0.650
0.550
0.450

3500. 3150. 2800. 2450.CM⁻¹
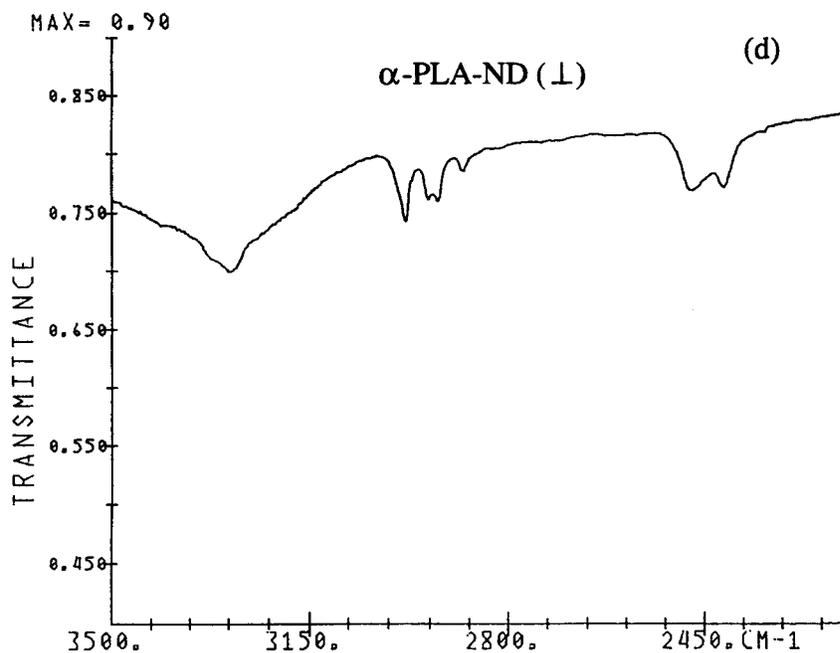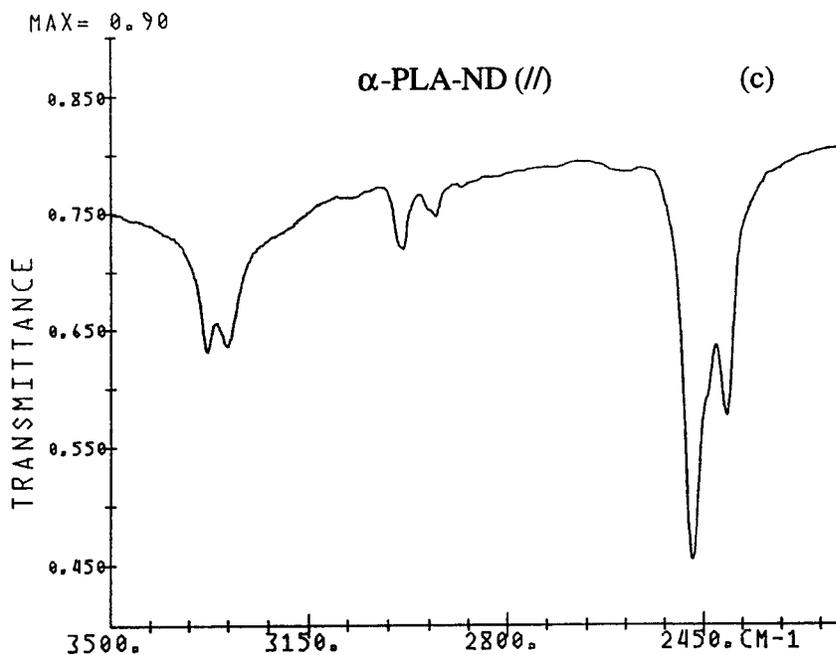
FIGURE 1 *(Continued from the previous page)*

polyethylene polarizer was used to obtain polarized far-ir spectra. Typical number of scans was 300 with 3 μm mylar film (700–140 cm^{-1}), 1000 with 6 μm mylar film (475–100 cm^{-1}), 2000 with 12 μm mylar film (240–50 cm^{-1}), and 4000 with 25 μm mylar film (125–25 cm^{-1}). As an ir source, a globar was used above the 100 cm^{-1} region while a mercury lamp was used below the 100 cm^{-1} region (with 25 μm mylar film).
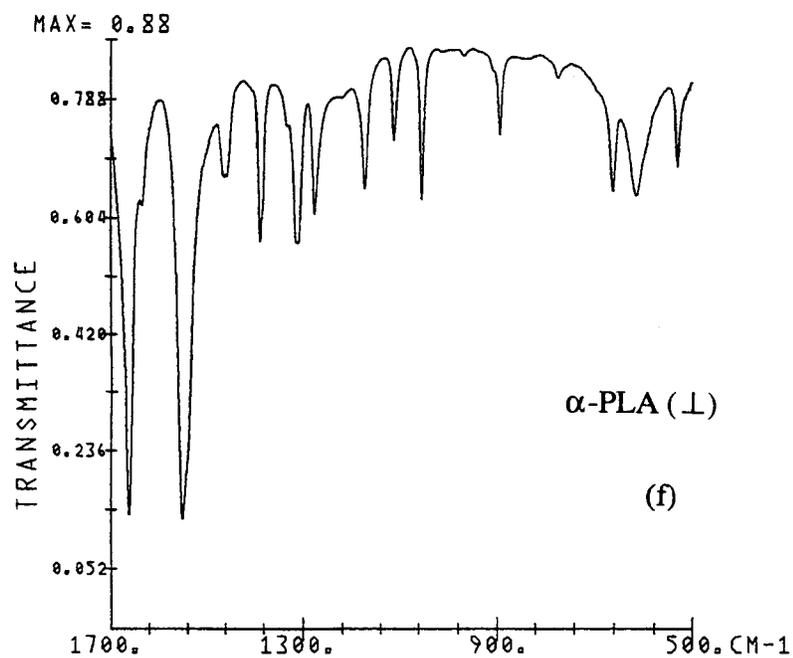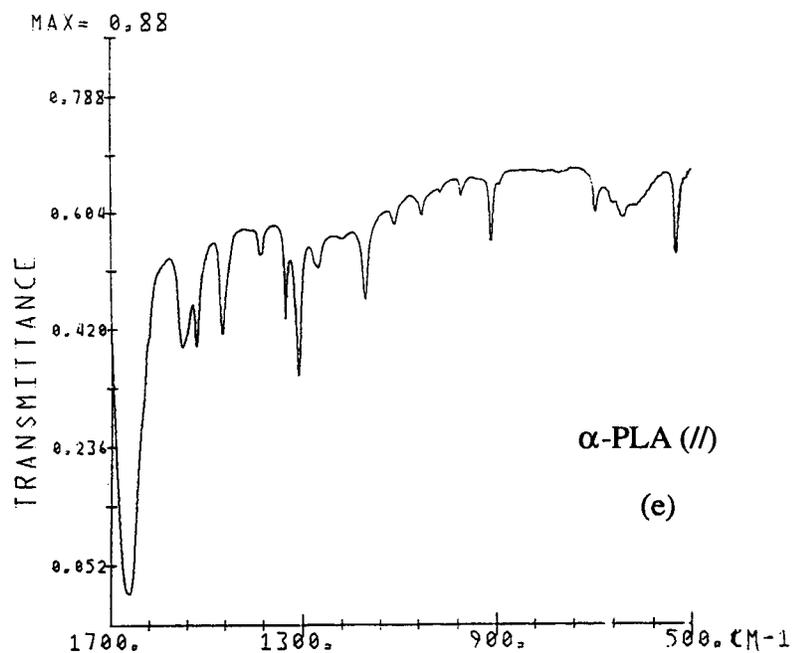
FIGURE 1   (*Continued from the previous page*)

COMPUTATION METHODS

The harmonic normal-mode frequencies of an infinite regular helix are calculated by diagonalizing a Hermitian matrix defined in mass-weighted Cartesian coordinates:

$$\mathbf{F}_m^X(\theta) \equiv \mathbf{M}^{-1/2}\mathbf{B}(\theta)^{\dagger}\mathbf{F}(\theta)\mathbf{B}(\theta)\mathbf{M}^{-1/2} \quad (1)$$
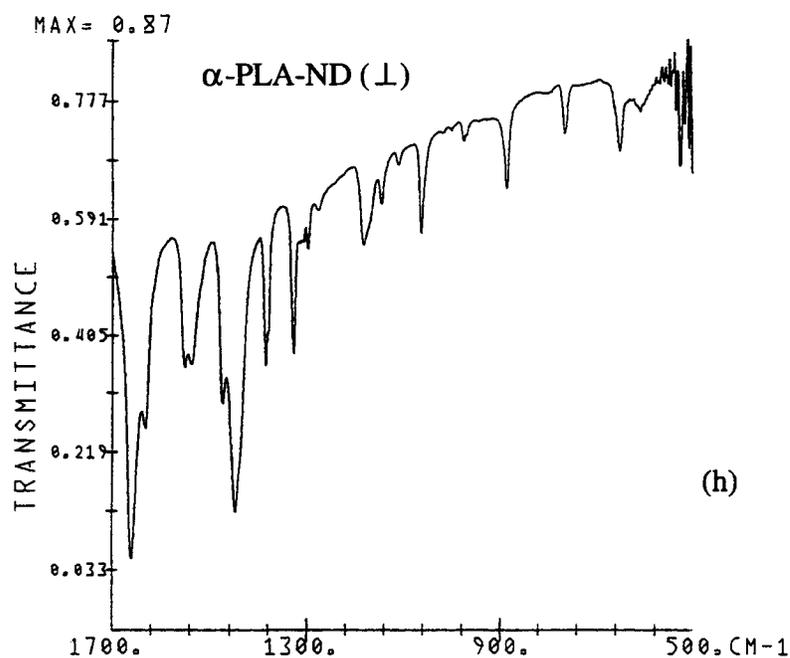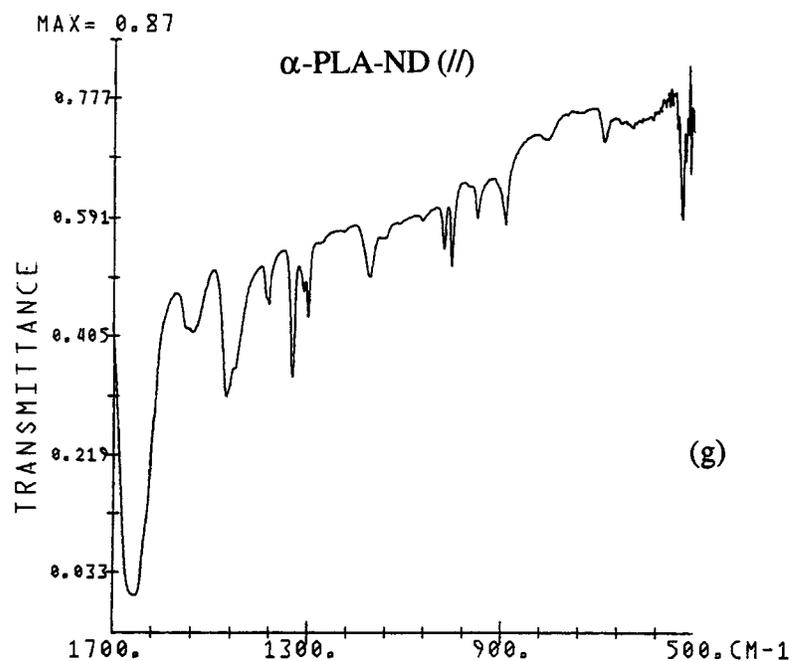
FIGURE 1   (*Continued from the previous page*)

where θ is the phase difference between adjacent groups, **M** is a diagonal matrix constructed from triads of the atomic masses in the reference group, and $\mathbf{F}(\theta)$ and $\mathbf{B}(\theta)$ are internal coordinate force constant matrix and B matrix, respectively, defined in helix symmetry coordinates.[21]

The force constant refinement was done by minimizing the quantity

MAX= 0.70

α-PLA (//)

(i)
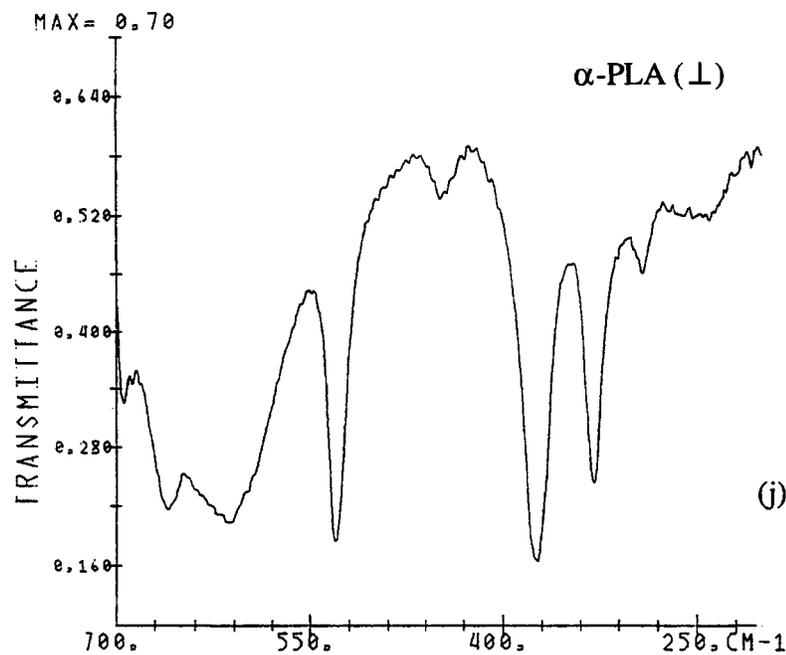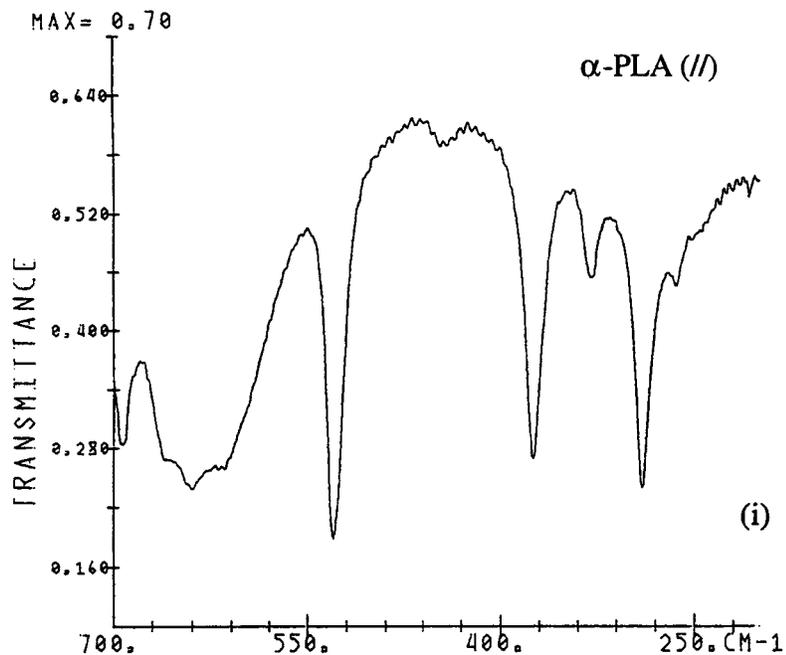
FIGURE 1 (*Continued from the previous page*)

$$\chi^2 \equiv \sum_{i=1}^{\text{NOFQ}} \{ w(i)(\nu_i^{\text{observed}} - \nu_i^{\text{calculated}}) \}^2 \quad (2)$$

where NOFQ is the total number of observed fre-

quencies (ν_i^{observed}) to be considered and $w(i)$ is the weight factor of the ith frequency. In order to facilitate the optimization of linearly dependent parameters, the actual minimizations of
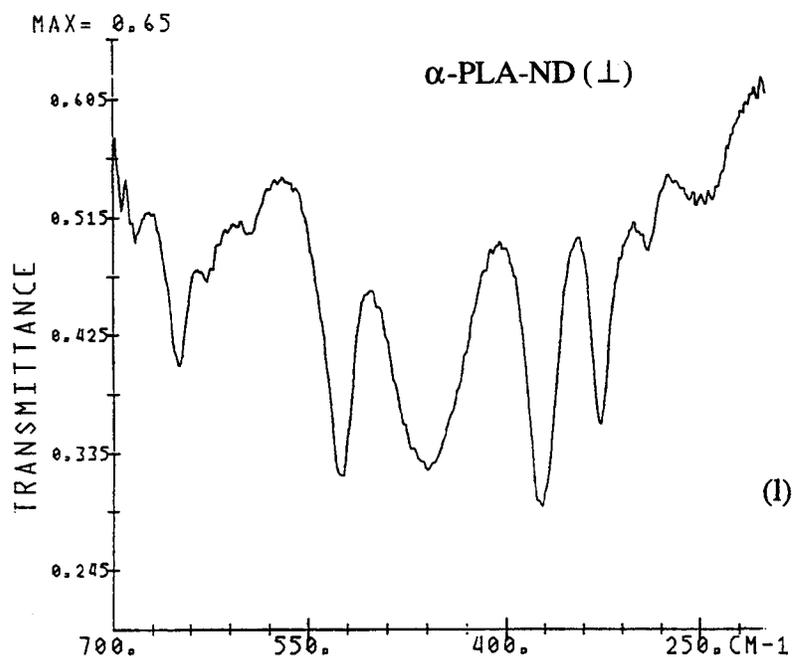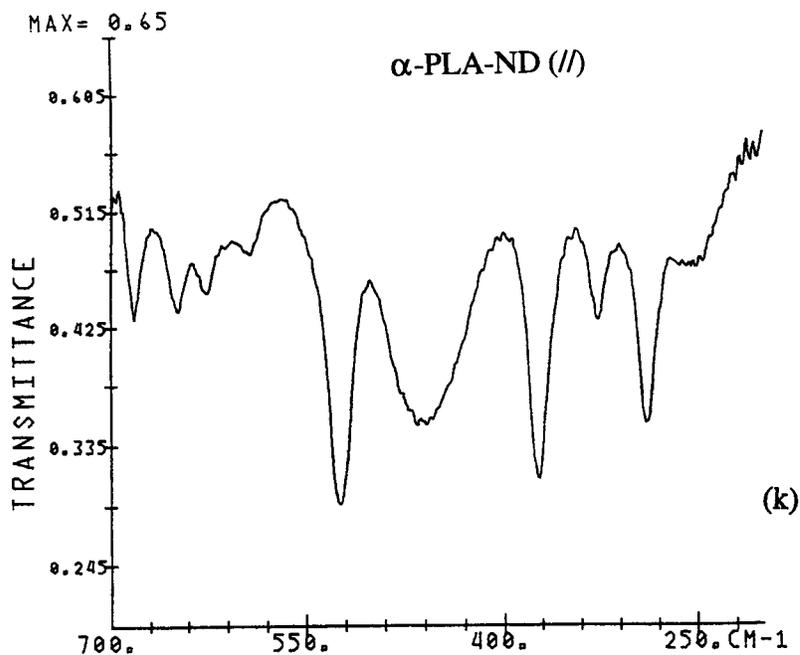
FIGURE 1 (*Continued from the previous page*)

Eq. (2) were done by the conjugate gradient method [29,30] with cubic interpolation in each line minimization by using a least-squares fitting program equipped also with the Levenberg–Marquardt method. [31,32]

NORMAL MODE CALCULATION

Structure and Coordinate Definitions

The structural parameters of α-PLA used in this study (Table I) are all the same as those used in
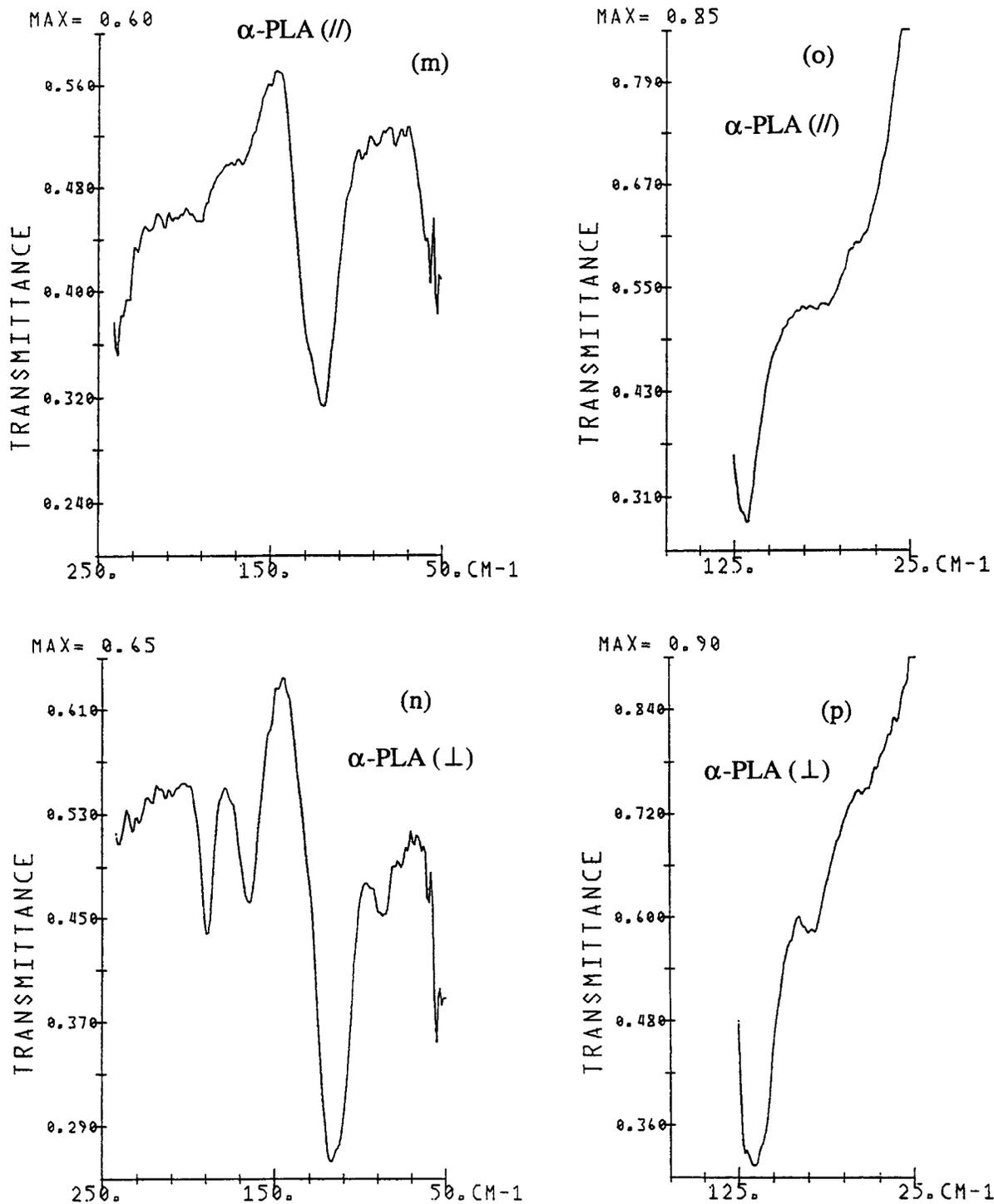
FIGURE 1 (*Continued from the previous page*)

the previous study by Dwivedi and Krimm.[18] Thus, the α-helix parameters are those of a 47/13 helix with a c-axis periodicity of 70.3 Å proposed by Brown and Trotter[33]: n (number of residues per turn) = 3.615 (a rotation per residue about the helix axis of δ = 99.57°) and h (rise per residue along the helix axis) = 1.495 Å. With the given helical parameters, bond lengths, bond angles, and peptide torsion angle ω (180° for *trans* peptide unit), there are in general two possible pairs of (ϕ,ψ).[34-36]

MAX= 0.70

(q)

α-PLA-ND (//)

MAX= 0.80

(s)

α-PLA-ND (//)

MAX= 0.70

(r)

α-PLA-ND (⊥)

MAX= 0.82

(t)

α-PLA-ND (⊥)
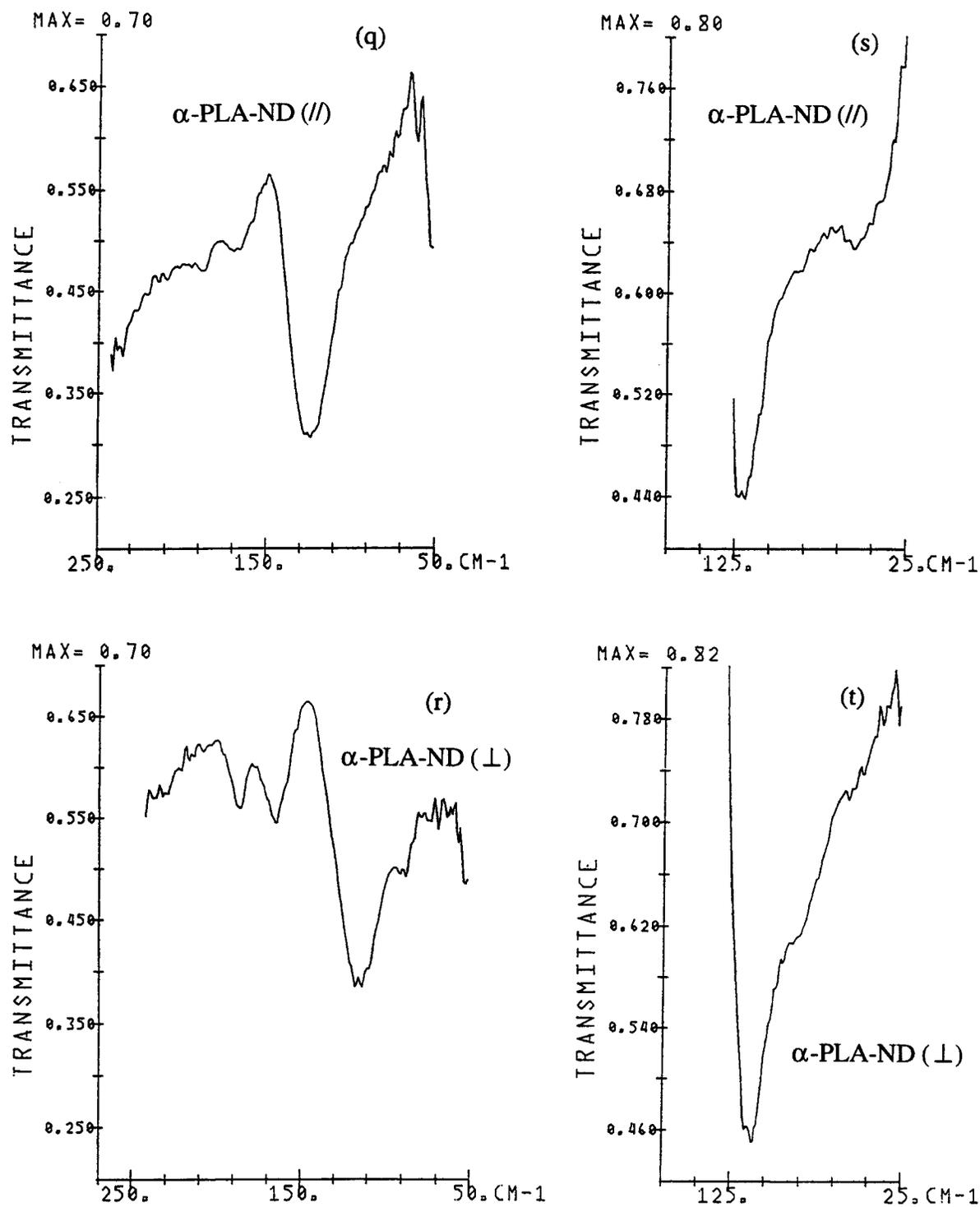
FIGURE 1 (*Continued from the previous page*)

Based on the above helical parameters, the $NC_\alpha C$ angle is adjusted to 109.87° in order to give the Arnott and Dover ϕ,ψ values[37] refined to the x-ray diffraction amplitudes. The structure corresponding

to the first pair, $(\phi,\psi) = (-57.37°, -47.49°)$, the values of Arnott and Dover, is called the α_I-helix (equivalent to the standard α-helix of Pauling and Corey[38]), and the structure corresponding to the

Table I Structural Parameters for α_I-PLA and α_{II}-PLA Helices

Parameter	α_I-PLA[a]	α_{II}-PLA[a]
n[b]	3.615	3.615
h[c]	1.495 Å	1.495 Å
(ϕ, ψ)	$(-57.37°, -47.49°)$	$(-70.47°, -35.75°)$
$d(\mathrm{H} \cdots \mathrm{O})$	1.882 Å	2.121 Å
$d(\mathrm{NO})$	2.857 Å	3.001 Å
$\angle(\mathrm{NH} \cdots \mathrm{O})$	164.19°	145.65°
$\angle(\mathrm{HNO})$	10.34°	23.51°
$\angle(\mathrm{CO} \cdots \mathrm{H})$	156.16°	136.62°
$\angle(\mathrm{CON})$	160.44°	145.81°

[a] Reference 18.
[b] Number of residues per turn.
[c] Rise per residue.

second pair, $(\phi, \psi) = (-70.47°, -35.75°)$, is called the α_{II}-helix.[39,40] Both pairs of (ϕ, ψ) fall within the stereochemically allowed region of the energy contour diagram.[41,42] According to a survey by Barlow and Thornton,[43] about 32% of all the amino acid residues in 57 known protein crystal structures are involved in α-helical structures with a mean helix length of 10 residues. The average (ϕ, ψ) values in α-helical segments was found to be $(-62°, -41°)$, thus falling about midway between the values for α_I and α_{II}. The orientation of the side chain methyl group is taken as the staggered position with respect to the backbone N atom, viz., a torsion angle about the $C_\alpha C_\beta$ bond of $\chi_1 = 60°$.

Since the α_I-helix has (ϕ, ψ) values refined to the well-defined x-ray structure of an α-PLA sample,[37] we assumed that this is the structure corresponding to our actually observed ir and Raman spectra of α-PLA, and the detailed normal mode analysis was done on this structure. According to the analysis of our new polarized ir spectra, especially in the amide A region,[44] there is another structure, in addition to the conventional α_I-helix, in our PLA samples that contain almost no residual DCA; proposals for this additional structure are considered elsewhere.[44] By using the resulting refined force field for α_I-PLA, detailed vibrational analyses can be done for other closely related helical structures, such as the α_{II}-helix and 3_{10}-helices.[43,45]

The internal coordinates for α-PLA are defined based on the atom numbering and the reference group (enclosed by a dashed line) as shown in Figure 2. Since the reference group, which is a basic chemical repeat unit chosen arbitrarily along the chain, contains ten atoms, there are a total of 30 normal modes in each symmetry species, with $28A$, $29E_1$, and $30E_2$ modes being optically active. Dif-

ferent from the previous analysis,[18] the intrachain hydrogen-bonded torsional displacements, namely, $\Delta\tau(\mathrm{CO})$ and $\Delta\tau(\mathrm{NH})$, are omitted in the list of internal coordinates of the reference group, since their corresponding force constants are presumed to be small enough to be neglected. For the calculation of higher order B-matrix elements and cubic anharmonic force constants in internal coordinates,[44] the two out-of-plane angle bend coordinates, CO ob and NH ob, are defined in the ordinary way,[46] different from the definition previously used in our group.[18,47] The internal and local symmetry coordinates of the reference group are defined in Tables II and III, respectively.

Force Field

The detailed list of ab initio NMA and peptide force constants and our initial values for the optimization are given elsewhere.[23] In order to compare the (scaled) ab initio force fields in Cartesian coordinates for various conformers of NMA and (L-Ala)$_2$, they were transformed into ones in the local symmetry coordinates defined in Table III. Every force constant name is labeled by an interaction type index: 0 = interaction within the reference group, i (positive) = interaction between the reference group and the ith group away from the reference group. When an interaction type index is greater than zero, the internal coordinate preceding the reference group is underlined in its force constant name. From this list[23] we can determine whether a peptide force constant depends on structure. We assume that the internal coordinate force constants that are not very sensitive to the local structures of small peptides are transferable to polypeptides like α-PLA. A structure-sensitive force constant (SSFC),
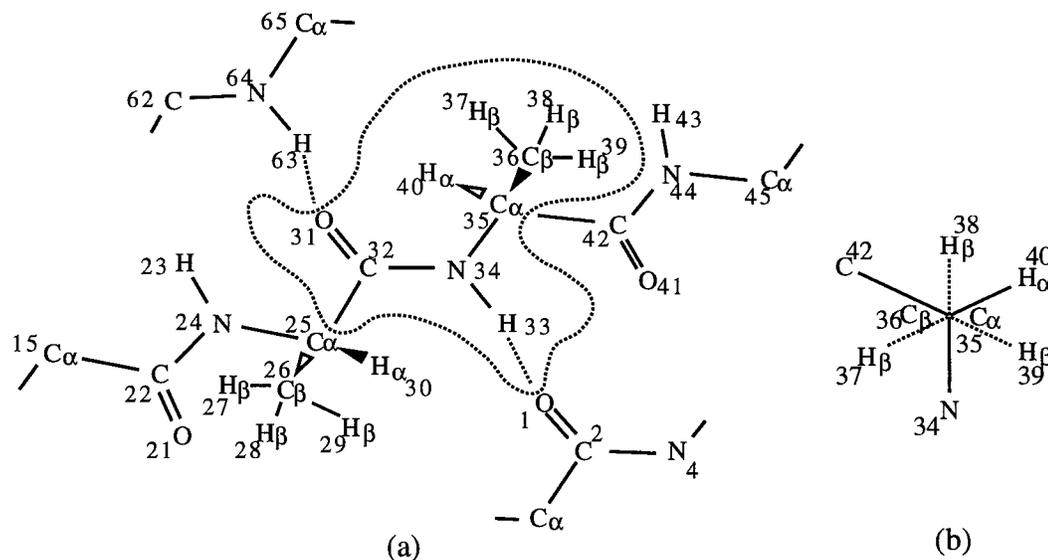
FIGURE 2   (a) A schematic drawing of α-PLA with atom numbering for coordinate definitions. A reference group (arbitrary) is enclosed by a dashed line. (b) Side chain residue orientation.

i.e., one that varies significantly between structures, cannot be directly transferred to other polypeptide structures, and it is labeled by an asterisk.

We observed that some of the SSFCs, specifically the interaction force constants between an angle bend or an out-of-plane angle bend of a peptide unit and angle bends around the adjacent C_α atom, certainly depend on the local dihedral angles. But the form of their explicit functional dependence could not be determined at this stage. Although an

Table II   Internal Coordinates of α-PLA

R	Name	Atoms	R	Name	Atoms
1	$\Delta r(C_\alpha C)$	25-32 (1.53 Å)[a]	20	$\Delta\theta(NC_\alpha C)$	34-35-42
2	$\Delta r(CO)$	32-31 (1.24 Å)	21	$\Delta\theta(C_\beta C_\alpha H_\alpha)$	36-35-40
3	$\Delta r(CN)$	32-34 (1.32 Å)	22	$\Delta\theta(C_\beta C_\alpha C)$	36-35-42
4	$\Delta r(NH)$	34-33 (1.00 Å)	23	$\Delta\theta(H_\alpha C_\alpha C)$	40-35-42
5	$\Delta r(NC_\alpha)$	34-35 (1.47 Å)	24	$\Delta\theta(C_\alpha C_\beta H_\beta^1)$	35-36-37
6	$\Delta r(C_\alpha C_\beta)$	35-36 (1.54 Å)	25	$\Delta\theta(C_\alpha C_\beta H_\beta^2)$	35-36-38
7	$\Delta r(C_\alpha H_\alpha)$	35-40 (1.07 Å)	26	$\Delta\theta(C_\alpha C_\beta H_\beta^3)$	35-36-39
8	$\Delta r(C_\beta H_\beta^1)$	36-37 (1.09 Å)	27	$\Delta\theta(H_\beta^1 C_\beta H_\beta^2)$	37-36-38
9	$\Delta r(C_\beta H_\beta^2)$	36-38 (1.09 Å)	28	$\Delta\theta(H_\beta^1 C_\beta H_\beta^3)$	37-36-39
10	$\Delta r(C_\beta H_\beta^3)$	36-39 (1.09 Å)	29	$\Delta\theta(H_\beta^2 C_\beta H_\beta^3)$	38-36-39
11	$\Delta r(H\cdots O)$	33-01	30	$\Delta\theta(CO\cdots H)$	32-31-63
12	$\Delta\theta(C_\alpha CO)$	25-32-31	31	$\Delta\theta(NH\cdots O)$	34-33-01
13	$\Delta\theta(C_\alpha CN)$	25-32-34	32	$\Delta\omega(CO)$[b]	32-31-25-34
14	$\Delta\theta(OCN)$	31-32-34	33	$\Delta\omega(NH)$	34-33-32-35
15	$\Delta\theta(CNH)$	32-34-33	34	$\Delta\tau(C_\alpha C)$	25-32
16	$\Delta\theta(CNC_\alpha)$	32-34-35	35	$\Delta\tau(CN)$	32-34
17	$\Delta\theta(HNC_\alpha)$	33-34-35	36	$\Delta\tau(NC_\alpha)$	34-35
18	$\Delta\theta(NC_\alpha C_\beta)$	34-35-36	37	$\Delta\tau(C_\alpha C_\beta)$	35-36
19	$\Delta\theta(NC_\alpha H_\alpha)$	34-35-40			

[a] The bond length of the equilibrium structure is shown in the parentheses.
[b] Out-of-plane angle bend defined as in Ref. 46.

Table III Local Symmetry Coordinates for α-PLA

S	Name[a]		S	Name	
1	$C_\alpha C$ s	R_1	18	H_α b2	$R_{19} - R_{23}$
2	CO s	R_2	19	C_β b1	$-R_{18} + 2 R_{20} - R_{22}$
3	CN s	R_3	20	C_β b2	$R_{18} - R_{22}$
4	NH s	R_4	21	CH_3 sb	$-R_{24} - R_{25} - R_{26} + R_{27} + R_{28} + R_{29}$
5	NC_α s	R_5	22	CH_3 ab1	$-R_{27} - R_{28} + 2 R_{29}$
6	$C_\alpha C_\beta$ s	R_6	23	CH_3 ab2	$R_{27} - R_{28}$
7	$C_\alpha H_\alpha$ s	R_7	24	CH_3 r1	$2 R_{24} - R_{25} - R_{26}$
8	$C_\beta H_\beta^1$ s	R_8	25	CH_3 r2	$R_{25} - R_{26}$
9	$C_\beta H_\beta^2$ s	R_9	26	$CO \cdots H$ b	R_{30}
10	$C_\beta H_\beta^3$ s	R_{10}	27	$NH \cdots O$ b	R_{31}
11	$H \cdots O$ s	R_{11}	28	CO ob	R_{32}
12	$C_\alpha CN$ d	$-R_{12} + 2 R_{13} - R_{14}$	29	NH ob	R_{33}
13	CO ib	$R_{12} - R_{14}$	30	$C_\alpha C$ t	R_{34}
14	CNC_α d	$-R_{15} + 2 R_{16} - R_{17}$	31	CN t	R_{35}
15	NH ib	$R_{15} - R_{17}$	32	NC_α t	R_{36}
16	$NC_\alpha C$ d	$R_{18} - R_{19} + R_{20} - R_{21} + R_{22} - R_{23}$	33	$C_\alpha C_\beta$ t	R_{37}
17	H_α b1	$-R_{19} + 2 R_{21} - R_{23}$			

[a] s: Stretch; d: deformation; b: angle bend; ib: in-plane angle bend; sb: symmetric angle bend; ab: antisymmetric angle bend; r: rock; ob: out-of-plane angle bend; and t: torsion.

SSFC cannot be directly transferable to other structures, in some cases we may infer whether its sign should be positive or negative; e.g., $f(CNC_\alpha$ d, C_β b2 0*), $f(CO$ ib, $NC_\alpha C$ d 1*), and $f(CO$ ib, C_β b1 1*) seem to be positive, while $f(NH$ ib, H_α b2 0*) and $f(CO$ ib, C_β b2 1*) seem to be negative (d: deformation; b: angle bend; ib: in-plane angle bend). All of our nonbonded interaction force constants had been neglected in the previous vibrational analyses, but ab initio results show that there are some non-negligible ones, and most of these are also structure sensitive. It should be noted that some of the nonbonded interaction force constants, especially those related to the transition dipole coupling (TDC) interaction, play a crucial role in the observed amide band splittings between different symmetry species.[21] The nonbonded interaction force constants will be discussed further in the analyses of the amide I and amide II bands.

In order to reduce the number of redundancies, which is inherent in force constants defined in internal coordinates, and to enhance transferability to other structures, the initial force field was defined and refined in local symmetry coordinates (Table III). Since we assume a complete local symmetry about the side chain methyl group, the following force constant relations related to the methyl group hold:

$$f(C_\beta H_\beta^1 \text{ s } 0) = f(C_\beta H_\beta^2 \text{ s } 0)$$
$$= f(C_\beta H_\beta^3 \text{ s } 0) \quad (3)$$

$$f(CH_3 \text{ ab1 } 0) = f(CH_3 \text{ ab2 } 0) \quad (4)$$

$$f(CH_3 \text{ r1 } 0) = f(CH_3 \text{ r2 } 0) \quad (5)$$

$$f(C_\beta H_\beta^1 \text{ s, } CH_3 \text{ sb } 0) = f(C_\beta H_\beta^2 \text{ s, } CH_3 \text{ sb } 0)$$
$$= f(C_\beta H_\beta^3 \text{ s, } CH_3 \text{ sb } 0) \quad (6)$$

$$f(C_\beta H_\beta^2 \text{ s, } CH_3 \text{ ab1 } 0)$$
$$= f(C_\beta H_\beta^3 \text{ s, } CH_3 \text{ ab1 } 0) \quad (7)$$

$$f(C_\beta H_\beta^2 \text{ s, } CH_3 \text{ ab2 } 0)$$
$$= -f(C_\beta H_\beta^3 \text{ s, } CH_3 \text{ ab2 } 0) \quad (8)$$

$$f(C_\beta H_\beta^2 \text{ s, } CH_3 \text{ r1 } 0)$$
$$= f(C_\beta H_\beta^3 \text{ s, } CH_3 \text{ r1 } 0) \quad (9)$$

$$f(C_\beta H_\beta^2 \text{ s, } CH_3 \text{ r2 } 0)$$
$$= -f(C_\beta H_\beta^3 \text{ s, } CH_3 \text{ r2 } 0) \quad (10)$$

(s: stretch; ab: antisymmetric angle bend; r: rock, sb: symmetric angle bend).

Twelve of the 121 nonzero force constants in the previous α_I-PLA force field,[18] viz., $f(CO$ t 0), $f(NH$ t 0), $f(CNC_\alpha$ d, H_α b2 0), $f(NH$ ib, H_α b1 0), $f(H_\alpha$ b1, C_β b1 0), $f(H_\alpha$ b2, C_β b1 0), $f(NC_\alpha C$ d, CH_3 sb 0), $f(NC_\alpha C$ d, CH_3 r2 0), $f(C_\beta$ b2, CH_3 sb 0), $f(C_\beta$ b2, CH_3 r1 0), $f(CO$ ob, H_α b1 1), and $f(NH$ ob, H_α b2 0) (t: torsion), were neglected in this work since they were found to be small from the ab initio calculations on small pep-

tides. A total of 170 force constants were considered as parameters to be fit to a total of 112 observed frequencies of α-PLA and α-PLA-ND. Considering the symmetry relations of Eqs. (3)–(10), it looks like at least 48 force constants have to be determined arbitrarily from a purely mathematical point of view. It would have been physically unrealistic to reduce the number of optimized force constants to the 112 observed data since, judging from the ab initio results on small peptides like NMA and (L-Ala)$_2$, the number of nonzero force constants required for a full description of α-PLA seems to exceed at least 200. We have chosen instead to optimize the force field so that the force constants do not stray from the general range indicated by the ab initio results. We feel this at least provides a reasonable set of constraints on the refinement process. Based on the ab initio results, except for some SSFCs (there are about 45 SSFCs among the 170 force constants), all the other force constants were kept within the boundaries of the ab initio prediction, with some force constants being kept constant at some point in the refinement process.

In the force field refinement procedure, there was no definite rule in determining the initial force constant values from the (scaled) ab initio ones. Overall, a rough average value of the (scaled) ab initio ones for various conformations was chosen as the initial force constant. Values from the conformations of (L-Ala)$_2$ close to the α-PLA structure were given more weight. Since we cannot neglect the effect due to the intrachain hydrogen-bonded structure in the α-helix, which is supposed to be significantly different from that of the (L-Ala)$_2$ conformers, the ab initio results for the (L-Ala)$_2$ conformation hydrogen bonded to four water molecules[28] was given more weight for some force constants. For the SSFCs, quite small initial values were assigned, and they were not varied until we reached the point of fairly good fitting in the whole frequency range. Since the ab initio hydrogen-bond-related force constants were still under improvement, we took moderate initial values for them based on the previous empirical analyses and they were not varied in the early stage of refinement. Some hydrogen-bond-related force constants and nonbonded interaction force constants, which tend to deviate significantly from the ab initio values, were manually adjusted to moderate values throughout the fitting processes. Fitting proceeded from the high frequency to the low frequency region. Since most of the low frequency modes are highly mixed and fairly well influenced by their corresponding high frequency modes, small values of weight factors were assigned

to the low frequency modes and high values were assigned to the well-assignable high frequency modes. After each fitting step, all varied force constants were compared to the ab initio values, and those that were significantly different from the corresponding ab initio values were fixed to reasonable values for the next step. The final set of refined force constants for α_I-PLA is given in Table IV.

RESULTS AND DISCUSSION

Calculated Frequencies and Phonon Dispersion Curves

Since we are dealing with only harmonic force constants, force field refinement was continued only until the differences between calculated and observed frequencies fell within ~ 5 cm^{-1} in the frequency range above 200 cm^{-1}. Considering the highly anharmonic nature of low frequency torsional and out-of-plane angle bend vibrations, further refinement is unwarranted. The calculated frequencies and diagonal potential energy distributions (PEDs) of the refined force field for α_I-PLA are listed in Table V together with the observed frequencies. The calculated dispersion curves [the frequencies, $\nu_i(\theta)$, as a function of the phase difference θ between adjacent groups] and the density of phonon states are shown in Figure 3.

The dispersion curves were obtained by computing normal-mode frequencies at an interval of $\Delta\theta = 2°$ in the positive half of the Brillouin zone ($0° \leq \theta \leq 180°$). The optically active modes occur at $\theta = 0°$ (A), $\theta = 99.57°$ (E_1), and $\theta = 199.14°$ (E_2), which are shown by dashed lines [the E_2 mode is at $\theta = 160.86°$ in the figure since $\nu_i(-\theta) = \nu_i(\theta)$ and $\nu_i(\theta + 360°) = \nu_i(\theta)$ from the symmetry]. The ν_2 and ν_3 branches (mainly CH$_3$ antisymmetric stretch, as) and the ν_8 and ν_9 branches (mainly CH$_3$ ab) are doubly degenerate. The two lowest energy dispersion curves, ν_{29} and ν_{30}, are acoustic branches. These branches are characterized by zero frequencies: the two zeros at $\theta = 0°$ (A) correspond to translation along (ν_{29} branch) and rotation about (ν_{30} branch) the helix axis, while the doubly degenerate zero at $\theta = 99.57°$ (E_1) corresponds to translations perpendicular to the helix axis.

The density of phonon states $g(\nu)$ was computed by counting the number of all fragments of $\Delta\theta = 2°$ width in the phase difference range $0° \leq \theta \leq 180°$ that fall within each frequency range of $\Delta\nu = 2$ cm^{-1} from 0 to 3400 cm^{-1}. The resulting num-

Table IV Refined Force Constants for α_I-PLA

Force Constant Name[a]	(i, j)[b]	Value	Force Constant Name	(i, j)[b]	Value
Diagonal force constants					
$C_\alpha C$ s 0	(1, 1)	4.1640	H_α b2 0	(18, 18)	0.6515
CO s 0	(2, 2)	10.2318	C_β b1 0	(19, 19)	1.2201
CN s 0	(3, 3)	6.7941	C_β b2 0	(20, 20)	0.9994
NH s 0	(4, 4)	5.9786	CH_3 sb 0	(21, 21)	0.5683
NC_α s 0	(5, 5)	5.3109	CH_3 ab1 0	(22, 22)	0.5337
$C_\alpha C_\beta$ s 0	(6, 6)	4.1009	CH_3 ab2 0	(23, 23)	0.5337
$C_\alpha H_\alpha$ s 0	(7, 7)	4.8324	CH_3 r1 0	(24, 24)	0.6603
$C_\beta H_\beta^1$ s 0	(8, 8)	4.8558	CH_3 r2 0	(25, 25)	0.6603
$C_\beta H_\beta^2$ s 0	(9, 9)	4.8558	$CO \cdots H$ b 0	(26, 26)	0.0100
$C_\beta H_\beta^3$ s 0	(10, 10)	4.8558	$NH \cdots O$ b 0	(27, 27)	0.0147
$H \cdots O$ s 0	(11, 11)	0.1410	CO ob 0	(28, 28)	0.5840
$C_\alpha CN$ d 0	(12, 12)	1.1561	NH ob 0	(29, 29)	0.1035
CO ib 0	(13, 13)	1.1860	$C_\alpha C$ t 0	(30, 30)	0.2780
CNC_α d 0	(14, 14)	0.8582	CN t 0	(31, 31)	0.3771
NH ib 0	(15, 15)	0.5490	NC_α t 0	(32, 32)	0.2849
$NC_\alpha C$ d 0	(16, 16)	1.1532	$C_\alpha C_\beta$ t 0	(33, 33)	0.0940
H_α b1 0	(17, 17)	0.6090			
Bonded interaction force constants					
$C_\alpha C$ s, CO s 0	(1, 2)	0.3992	NC_α s, CH_3 r1 0	(5, 24)	−0.0232
$C_\alpha C$ s, CN s 0	(1, 3)	0.2675	NC_α s, CH_3 r2 0	(5, 25)	0.0559
$\underline{C_\alpha C\ s,\ NC_\alpha\ s}$ 1	(<u>1</u>, 5)	0.2073	CO s, $CO \cdots H$ b 0	(2, 26)	0.0420
$\underline{C_\alpha C\ s,\ C_\alpha C_\beta\ s}$ 1	(<u>1</u>, 6)	0.1360	NH s, $NH \cdots O$ b 0	(4, 27)	0.0097
CO s, CN s 0	(2, 3)	1.1269	$C_\alpha CN$ d, CO ib 0	(12, 13)	0.1420
CN s, NC_α s 0	(3, 5)	0.2005	$C_\alpha CN$ d, CNC_α d 0	(12, 14)	−0.0470
NC_α s, $C_\alpha C_\beta$ s 0	(5, 6)	0.1724	$C_\alpha CN$ d, NH ib 0	(12, 15)	0.0150
NC_α s, $C_\alpha H_\alpha$ s 0	(5, 7)	0.0903	CO ib, CNC_α d 0	(13, 14)	0.0542
$C_\alpha C_\beta$ s, $C_\alpha H_\alpha$ s 0	(6, 7)	0.0458	CO ib, NH ib 0	(13, 15)	−0.0582
$C_\alpha C_\beta$ s, $C_\beta H_\beta^1$ s 0	(6, 8)	0.0435	CNC_α d, NH ib 0	(14, 15)	−0.0270
$C_\alpha C_\beta$ s, $C_\beta H_\beta^2$ s 0	(6, 9)	0.0435	CNC_α d, $NC_\alpha C$ d 0*	(14, 16)	−0.0120
$C_\alpha C\beta$ s, $C_\beta H_\beta^3$ s 0	(6, 10)	0.0435	CNC_α d, H_α b1 0*	(14, 17)	0.0440
$C_\beta H_\beta^1$ s, $C_\beta H_\beta^2$ s 0	(8, 9)	0.0576	CNC_α d, C_β b1 0*	(14, 19)	−0.0022
$C_\beta H_\beta^1$ s, $C_\beta H_\beta^3$ s 0	(8, 10)	0.0576	CNC_α d, C_β b2 0*	(14, 20)	0.1004
$C_\beta H_\beta^2$ s, $C_\beta H_\beta^3$ s 0	(9, 10)	0.0576	NH ib, $NC_\alpha C$ d 0*	(15, 16)	0.0322
$\underline{H \cdots O\ s,\ CO\ s}$ 3	(<u>11</u>, 2)	0.0100	NH ib, H_α b2 0*	(15, 18)	−0.0364
NH s, $H \cdots O$ s 0	(4, 11)	0.0127	NH ib, C_β b1 0*	(15, 19)	0.0205
$C_\alpha C$ s, $C_\alpha CN$ d 0	(1, 12)	0.2945	$\underline{C_\alpha CN\ d,\ NC_\alpha C\ d}$ 1*	(<u>12</u>, 16)	0.0360
$C_\alpha C$ s, CO ib 0	(1, 13)	0.2564	$\underline{C_\alpha CN\ d,\ H_\alpha\ b1}$ 1*	(<u>12</u>, 17)	−0.0560
CO s, $C_\alpha CN$ d 0	(2, 12)	−0.4322	$\underline{C_\alpha CN\ d,\ H_\alpha\ b2}$ 1*	(<u>12</u>, 18)	−0.0976
CO s, CO ib 0	(2, 13)	−0.0892	$\underline{C_\alpha CN\ d,\ C_\beta\ b1}$ 1*	(<u>12</u>, 19)	−0.0150
CO s, NH ib 0	(2, 15)	0.0380	$\underline{CO\ ib,\ NC_\alpha C\ d}$ 1*	(<u>13</u>, 16)	0.0460
CN s, $C_\alpha CN$ d 0	(3, 12)	0.1029	$\underline{CO\ ib,\ H_\alpha\ b1}$ 1*	(<u>13</u>, 17)	0.0280
CN s, CO ib 0	(3, 13)	−0.4184	$\underline{CO\ ib,\ H_\alpha\ b2}$ 1*	(<u>13</u>, 18)	0.0195
CN s, CNC_α d 0	(3, 14)	0.1918	$\underline{CO\ ib,\ C_\beta\ b1}$ 1*	(<u>13</u>, 19)	0.1200
CN s, NH ib 0	(3, 15)	0.1549	$\underline{CO\ ib,\ C_\beta\ b2}$ 1*	(<u>13</u>, 20)	−0.0580
NH s, $C_\alpha CN$ d 0	(4, 12)	−0.0548	$NC_\alpha C$ d, H_α b1 0	(16, 17)	0.0660
NH s, CNC_α d 0	(4, 14)	−0.0440	$NC_\alpha C$ d, H_α b2 0	(16, 18)	−0.0529
NC_α s, $C_\alpha CN$ d 0	(5, 12)	0.0270	$NC_\alpha C$ d, C_β b1 0	(16, 19)	0.0555
NC_α s, CO ib 0	(5, 13)	0.0692	$NC_\alpha C$ d, C_β b2 0*	(16, 20)	−0.0167
NC_α s, CNC_α d 0	(5, 14)	0.2825	H_α b1, H_α b2 0*	(17, 18)	−0.0062

Table IV (*Continued from the previous page*)

Force Constant Name[a]	(i, j)[b]	Value	Force Constant Name	(i, j)[b]	Value
NC_α s, NH ib 0	(5, 15)	−0.1562	H_α b2, C_β b2 0*	(18, 20)	0.0404
$\underline{C_\alpha CN}$ d, NC_α s 1*	(12, 5)	−0.0220	C_β b1, C_β b2 0*	(19, 20)	−0.0722
$\underline{CO}$ ib, NC_α s 1*	(13, 5)	0.0634	$NC_\alpha C$ d, CH_3 r1 0	(16, 24)	−0.0960
NC_α s, NC_α C d 0	(5, 16)	0.1839	H_α b1, CH_3 sb 0	(17, 21)	−0.0190
NC_α s, H_α b1 0	(5, 17)	−0.1993	H_α b1, CH_3 r1 0	(17, 24)	0.0623
NC_α s, H_α b2 0	(5, 18)	0.2607	C_β b1, CH_3 sb 0	(19, 21)	0.0228
NC_α s, C_β b1 0	(5, 19)	0.2255	C_β b1, CH_3 r1 0	(19, 24)	0.0480
NC_α s, C_β b2 0	(5, 20)	0.3520	C_β b1, CH_3 r2 0	(19, 25)	−0.0324
$C_\alpha C_\beta$ s, $NC_\alpha C$ d 0	(6, 16)	0.1602	C_β b2, CH_3 ab 2 0	(20, 23)	−0.0300
$C_\alpha C_\beta$ s, H_α b1 0	(6, 17)	0.2108	C_β b2, CH_3 r2 0	(20, 25)	0.1158
$C_\alpha C_\beta$ s, C_β b1 0	(6, 19)	−0.2671	$\underline{CO}$ ob, $NC_\alpha C$ d 1*	(28, 16)	−0.0480
$C_\alpha C_\beta$ s, C_β b2 0	(6, 20)	−0.0600	$\underline{CO}$ ob, H_α b2 1*	(28, 18)	0.0340
$C_\alpha H_\alpha$ s, $NC_\alpha C$ d 0	(7, 16)	−0.1120	$\underline{CO}$ ob, C_β b1 1*	(28, 19)	0.0359
$\underline{C_\alpha C}$ s, $NC_\alpha C$ d 1	(1, 16)	0.1760	$\underline{CO}$ ob, C_β b2 1*	(28, 20)	−0.0457
$\underline{C_\alpha C}$ s, H_α b1 1	(1, 17)	−0.1080	NH ob, $NC_\alpha C$ d 0*	(29, 16)	−0.0190
$\underline{C_\alpha C}$ s, H_α b2 1	(1, 18)	−0.1300	NH ob, H_α b1 0*	(29, 17)	−0.0260
$\underline{C_\alpha C}$ s, C_β b1 1	(1, 19)	0.2100	NH ob, C_β b1 0*	(29, 19)	−0.0156
$\underline{C_\alpha C}$ s, C_β b2 1	(1, 20)	−0.2003	NH ob, C_β b2 0*	(29, 20)	−0.0240
$C_\alpha C_\beta$ s, CH_3 sb 0	(6, 21)	−0.2772	CO ob, CO···H 0	(28, 26)	0.0140
$C_\beta H_\beta^1$ s, CH_3 sb 0	(8, 21)	0.0529	NH ob, NH···O 0	(29, 27)	0.0040
$C_\beta H_\beta^1$ s, CH_3 ab1 0	(8, 22)	−0.1280	CO ob, NH ob 0	(28, 29)	−0.0140
$C_\beta H_\beta^1$ s, CH_3 r1 0	(8, 24)	0.0706	CO ob, CN t 0	(28, 31)	−0.0290
$C_\beta H_\beta^2$ s, CH_3 sb 0	(9, 21)	0.0529	CO ob, NC_α t 0	(28, 32)	−0.0221
$C_\beta H_\beta^2$ s, CH_3 ab1 0	(9, 22)	0.0578	$\underline{CO}$ ob, NC_α t 1*	(28, 32)	0.0280
$C_\beta H_\beta^2$ s, CH_3 ab2 0	(9, 23)	0.0717	NH ob, $C_\alpha C$ t 0	(29, 30)	0.0300
$C_\beta H_\beta^2$ s, CH_3 r1 0	(9, 24)	−0.0394	$\underline{C_\alpha C}$ t, NH ob 1*	(30, 29)	−0.0180
$C_\beta H_\beta^2$ s, CH_3 r2 0	(9, 25)	0.0758	NH ob, CN t 0	(29, 31)	−0.0250
$C_\beta H_\beta^3$ s, CH_3 sb 0	(10, 21)	0.0529	NH ob, NC_α t 0*	(29, 32)	0.0261
$C_\beta H_\beta^3$ s, CH_3 ab1 0	(10, 22)	0.0578	$C_\alpha C$ t, CN t 0	(30, 31)	0.0675
$C_\beta H_\beta^3$ s, CH_3 ab2 0	(10, 23)	−0.0717	$\underline{C_\alpha C}$ t, NC_α t 1	(30, 32)	0.0860
$C_\beta H_\beta^3$ s, CH_3 r1 0	(10, 24)	−0.0394	CN t, NC_α t 0	(31, 32)	0.1090
$C_\beta H_\beta^3$ s, CH_3 r2 0	(10, 25)	−0.0758			
Nonbonded interaction force constants					
$\underline{NH}$ s, CO s 3*	(4, 2)	−0.0286	$\underline{CN}$ s, CO s 3*	(3, 2)	0.0530
CO s, NC_α s 0*	(2, 5)	−0.0935	$\underline{CN}$ s, NC_α s 1*	(3, 5)	0.0898
$\underline{CO}$ s, NC_α s 1*	(2, 5)	0.0210	$\underline{CN}$ s, CN s 1*	(3, 3)	−0.0340
$\underline{CO}$ s, CO s 1*	(2, 2)	0.0400	$\underline{CN}$ s, CN s 2*	(3, 3)	−0.0510
$\underline{CO}$ s, CO s 3*	(2, 2)	−0.0340	$\underline{NH}$ ib, NH ib 1*	(15, 15)	−0.0070
$\underline{CO}$ s, CN s 1*	(2, 3)	−0.0180	$\underline{NH}$ ib, NH ib 3*	(15, 15)	0.0010

 [a] s: Stretch; d: deformation; b: angle bend; sb: symmetric angle bend; ab: antisymmetric angle bend; r: rock; ib: in-plane angle bend; ob: out-of-plane angle bend; t: torsion. Every force constant is labeled by an interaction type index: 0: interaction within the reference group; *i*: interaction between the reference group and the *i*th group away from the reference group. When the interaction type index is greater than zero, the internal coordinate preceding the reference group is underlined in its force constant name. Interaction force constants sensitive to changes in local structure are labeled by an asterisk.
[b] Symmetry coordinates (Table III) connected by force constant.

ber for each $\Delta\nu$ was divided by 91 in order to normalize $g(\nu)$, namely

$$\int_0^\infty g(\nu)\, d\nu = 3p(= 30) \qquad (11)$$

where p is the number of atoms in the reference group.

In Table VI we list the main peaks in the calculated phonon density of states below 700 cm^{-1}, with corresponding PEDs at each peak position.

Table V Observed and Calculated Vibrational Frequencies (in cm^{-1}) of α_{I}-PLA

α_{I}-PLA								
Observed Frequencies[a]					Calculated Frequencies			
Raman			IR					
A	E_1	E_2	A	E_1	A	E_1	E_2	Potential Energy Distribution[b]
							3314	NH s(98)
				3321MS		3314		NH s(98)
3311MS			3321VS[c]		3314			NH s(98)
				3290M				NH s(E_1) of additional structure
3288M			3283S					NH s(A) of additional structure
			3070MW					2 × [1548VS(E_1)] = 3096(A)
			3062sh					2 × [1539sh(E_1)] = 3078(A)
			3028W					2 × [1518W(A)] = 3036(A)
2989S			2987M		2989			BHb2 s(52), BHb3 s(50)
	2989S					2989		BHb2 s(52), BHb3 s(50)
		2988S					2989	BHb2 s(52), BHb3 s(50)
					2987			BHb1 s(68), BHb3 s(18), BHb2 s(16)
				2981M		2987		BHb1 s(68), BHb3 s(18), BHb2 s(16)
							2987	BHb1 s(68), BHb3 s(18), BHb2 s(16)
							2970	AHa s(100)
	2970sh					2970		AHa s(100)
					2970			AHa s(100)
2941VS[d]			2929MW		2930			BHb1 s(33), BHb2 s(33), BHb3 s(32)
	2941S			2940MW		2930		BHb1 s(33), BHb2 s(33), BHb3 s(32)
		2941S					2930	BHb1 s(33), BHb2 s(33), BHb3 s(32)
2882M	2882M	2881M	2881W	2881MW				1461MS(A) + 1454M(E_1) = 2915(E_1)
			2818W					1274M(E_1) + 1548VS(E_1) = 2822(A); 1305S(A) + 1518W(A) = 2823(A)
			2781VW					1266W(A) + 1518W(A) = 2784(A)
2747MW	2747W	2745W						1460MS(A) + 1306S(A) = 2766(A)
	1665MW						1665	CO s(78), ACN d(11)
				1659S		1661		CO s(80), ACN d(11)
1656VS			1658VS		1658			CO s(83), ACN d(11)
				1632sh				891(E_1) + 752(A) = 1643(E_1); β structure (?)
							1552	NH ib(60), CN s(33), NA s(10)

Table V (*Continued from the previous page*)

				α_1-PLA				
	Observed Frequencies[a]				Calculated Frequencies			
	Raman			IR				
A	E_1	E_2	A	E_1	A	E_1	E_2	Potential Energy Distribution[b]
				1548VS	1547			NH ib(58), CN s(35), NA s(10)
				1539sh				NH ib(E_1) of additional structure
			1518W		1521			NH ib(59), CN s(33), NA s(10)
1460MS			1461MS		1460			CH3 ab2(86), CH3 r2(10)
				1461MW		1460		CH3 ab2(86)
							1459	CH3 ab2(86)
		1454S					1456	CH3 ab1(91)
	1456MS			1454M		1456		CH3 ab1(91)
					1455			CH3 ab1(91)
							1381	CH3 sb(98), AB s(10)
				1384MS		1381		CH3 sb(99), AB s(10)
1381MW			1380W		1381			CH3 sb(100), AB s(10)
		1337M					1338	AC s(21), Ha b2(20), NH ib(15), Ha b1(11)
	1334sh						1334	Ha b2(31), AC s(19), NH ib(11), Ha b1(10)
1331S			1330M		1328			Ha b2(57), AC s(14)
	1313sh			1310M		1311		Ha b2(35), Ha b1(23), CN s(10)
							1309	Ha b2(57), CN s(10)
1306S			1305S		1305			Ha b1(55)
		1285MW					1283	Ha b1(57), NH ib(11)
	1275MW			1274M		1278		Ha b1(42), NH ib(15)
1264MW			1266W		1263			NH ib(23), CN s(17), Ha b1(16), AC s(12), Ha b2(12)
				1171MS		1169		NA s(44), CH3 r1(12)
							1169	NA s(42), CH3 r1(16), NAC d(10)
1167MS			1168M		1169			NA s(49), CH3 r2(14), Ha b2(13)
	1108MS			1109M		1110		AB s(24), CH3 r1(24)
1106S			1108W		1110			CH3 r1(34), AB s(24), NAC d(11)
		1106S					1107	AB s(28), CH3 r1(16), B b1(10)
1094W								β structure (?)
		1070MW					1068	CH3 r2(41), CH3 r1(12)
	1051W			1050MS		1051		CH3 r2(33), AB s(15)
1015W			1012VW		1013			AB s(29), CH3 r2(15), CH3 r1(14), Ha b1(11), CN s(11)
966MW			970W		970			CH3 r2(44), AC s(18), NA s(14), AB s(13)
	942VW						943	CH3 r2(30), NA s(14), CN s(11)

Table V   (*Continued from the previous page*)

α₁-PLA								
Observed Frequencies[a]					Calculated Frequencies			
Raman			IR					
A	E₁	E₂	A	E₁	A	E₁	E₂	Potential Energy Distribution[b]
		930MW					932	CH3 r2(26), CN s(15), NA s(14), CH3 r1(12), CNA d(11)
908VVS			908M		909			CNA d(19), CO ib(16), CH3 r1(12)
	892sh			891M		892		AB s(22), CH3 r1(21), CO ib(16)
		882MW					882	AB s(38), CH3 r1(21), CO ib(15)
	771VW			772MW		773		CO ob(53), B b1(12)
							764	CO ob(62), B b1(14)
752MW		(753MW)[e]			752			CO ob(68)
693MW		(693MW)[e]	693MW		695			NAC d(41), ACN d(23), CH3 r1(18)
		661MW					665	CO ib(20), AC s(19), NH ob(17)
				659MS		661		NAC d(13), NH ob(12), NA t(12), CN t(11), CO ob(11), AC s(10), ACN d(10)
638MW			639M		635			NH ob(56), CN t(52), NA t(34), NH:O b(13)
				612MS		616		CN t(46), NH ob(40), NA t(26), NH:O b(10)
							612	CN t(55), NH ob(33), NA t(32), NH:O b(10)
530VS			529MS		530			CO ib(27), AC s(21), ACN d(14), AB s(12)
	530MS			528M		527		NAC d(28), CO ib(17), AC s(17)
		530S					518	NAC d(34), AC s(15)
		374MS					374	B b1(26), B b2(18), NAC d(11)
375M			374M		372			B b1(28), CO ib(21), CNA d(12), NAC d(11)

Table V (*Continued from the previous page*)

				α_I-PLA				
Observed Frequencies[a]					Calculated Frequencies			
Raman			IR					
A	E_1	E_2	A	E_1	A	E_1	E_2	Potential Energy Distribution[b]
	374M			373M	371			B b1(29), CO ib(23), CNA d(15)
	329W			328MW	327			B b2(49), ACN d(16)
		311M					314	CO ib(23), CNA d(21), B b2(19), NAC d(16), ACN d(15)
290VW		(290MW)[e]	289M		291			B b2(41), B b1(12), CO ib(12)
263MS			263VW		266			B b2(33), AC t(13), AB t(11)
							229	AB t(89)
						229		AB t(82)
					217			AB t(84)
		209M					208	B b2(37), ACN d(14), B b1(11), NH ob(10), AB t(10)
	189M			188MW	197			B b1(16), B b2(16), AB t(10)
	163M			163MW	172			CNA d(26), AC t(23), ACN d(15), NAC d (10)
		162M					162	NH ob(29), NA t(17), CNA d(12)
					151			ACN d(24), NAC d(20), CNA d(19), AC t(18), NA t(15)
				116M	125			AC t(22), NA t(21), CN t(18), B b2(10)
119sh			119M		118			AC t(24), NA t(17), CN t(14), CNA d(14), H:O s(13)
		84M		(84VW)[f]			95	CN t(35), AC t(26), CNA d(14)
		60sh					75	AC t(32), B b1(14), NA t(14)
							47	AC t(66), NA t(36), H:O s(29), NH ob(25)
						41		CN t(26), AC t(24), NH ob(18), NA t(12), H:O s(11)

Table V (*Continued from the previous page*)

				α_I-PLA-ND				
	Observed Frequencies[a]				Calculated Frequencies			
Raman			IR					
A	E_1	E_2	A	E_1	A	E_1	E_2	Potential Energy Distribution[b]
			2989sh		2989			BHb2 s(52), BHb3 s(50)
						2989		BHb2 s(52), BHb3 s(50)
							2989	BHb2 s(52), BHb3 s(50)
			2983M		2987			BHb1 s(68), BHb3 s(18), BHb2 s(16)
				2979M		2987		BHb1 s(68), BHb3 s(18), BHb2 s(16)
							2987	BHb1 s(68), BHb3 s(18), BHb2 s(16)
							2970	AHa s(100)
				2970sh		2970		AHa s(100)
					2970			AHa s(100)
			2927W		2930			BHb1 s(33), BHb2 s(33), BHb3 s(32)
				2940MW		2930		BHb1 s(33), BHb2 s(33), BHb3 s(32)
							2930	BHb1 s(33), BHb2 s(33), BHb3 s(32)
				2473W		2433		ND s(97)
							2432	ND s(97)
			2468S[g]		2432			ND s(97)
				2447W				ND s(E_1) of additional structure
			2438sh					ND s(A) of the additional structure
				2414W				
			2406MS					1429(A) + 1000M(A) = 2429(A)
							1657	CO s(82), CN s(10), ACN d(10)
	1659MS			1658S	1654			CO s(83), CN s(12), ACN d(10)
1647VS			1648VS		1650			CO s(86), CN s(11), ACN d(10)
				1627sh				882(E_1) + 751(A) = 1633(E_1); β structure (?)
							1471	CH3 ab2(36), CN s(27), NA s(14), AC s(11)
	1471sh			1472M		1469		CH3 ab2(36), CN s(27), NA s(11), AC s(10)
1461MS			1465M		1460			CH3 ab2(82)
1453sh					1457			CH3 ab1(83)
	1457S						1456	CH3 ab1(74), CH3 ab2(16)
		1455S					1456	CH3 ab1(89)
	1444sh			1445S	1449			CH3 ab2(37), CN s(25), CH3 ab1(14)
							1448	CH3 ab2(51), CN s(24)

Table V (*Continued from the previous page*)

				α_I-PLA-ND				
	Observed Frequencies[a]				Calculated Frequencies			
	Raman			IR				
A	E_1	E_2	A	E_1	A	E_1	E_2	Potential Energy Distribution[b]
1429sh		(1429W)[e]			1429			CN s(49), ND ib(17), NA s(15), CO ib(15), AC s(11)
		1382MW					1381	CH3 sb(100), AB s(10)
				1382M		1381		CH3 sb(100), AB s (10)
1379MW			1377MW		1381			CH3 sb(100), AB s(10)
1327S			1327M		1328			Ha b2(58), AC s(15)
	1327MS			1323M		1324		Ha b2(60)
		1324MS					1321	Ha b2(59), Ha b1(10)
		1296M					1297	Ha b1(57), Ha b2(20)
	1296M			1295W		1296		Ha b1(65), Ha b2(13)
1296M			1295MW		1294			Ha b1(73)
				1179MW		1175		NA s(32), AC s(16)
1171M			1168MW		1174			NA s(39), Ha b2(18), AC s(14), CH3 r2(10)
							1174	NA s(28), AC s(17), ND ib(11), Ha b1(11)
							1149	CH3 r1(22), CH3 r2(13)
	1142sh			1144W		1143		CH3 r1(30), NAC d(11)
1134M			1134VW		1135			CH3 r1(39), NAC d(15), AB s(11)
							1075	CH3 r2(28), AB s(20), CH3 r1(19)
	1062MW			1061M		1060		CH3 r2(26), AB s(23), CH3 r1(14)
1017VW			1016MW		1015			AB s(45), Ha b1(10)
1001MS			1000M		1001			CH3 r2(37), ND ib(23)
	973M			974W		975		ND ib(49), CN s(11)
		968M					970	ND ib(56), CN s(10), CH3 r2(10)
946S			946MW		942			ND ib(23), CH3 r2(16), AC s(12), CN s(10), NA s(10)
	936sh					931		CH3 r2(27), NA s(15)
		922W					920	CH3 r2(24), NA s(16), CN s(15), CH3 r1(13), CNA d(10)
888VVS			887M		888			CO ib(17), CNA d(17), CH3 r1(14), NA s(11)
				882M		883		CH3 r1(20), AB s(17), CO ib(16)
		878sh					880	AB s(36), CH3 r1(18), CO ib(15)
	764W			764M		766		CO ob(55), B b1(11)
							759	CO ob(63), B b1(14)
751W		(753MW)[e]			748			CO ob(70)

Table V (*Continued from the previous page*)

	α₁-PLA-ND							
Observed Frequencies[a]					Calculated Frequencies			
Raman			IR					
A	E_1	E_2	A	E_1	A	E_1	E_2	Potential Energy Distribution[b]
685W		(685M)[e]	682MW		684			NAC d(39), ACN d(21), CH3 r1(15)
		655M					651	CO ib(25), AC s(20), NAC d(13)
				649M		646		NAC d(19), CO ob(15), AC s(13), ACN d(13), CO ib(12)
524VS			523MS		527			CO ib(26), ACN d(18), AC s(18), AB s(10)
	525VS			524M		521		NAC d(28), AC s(17), CO ib(16)
		525VS					515	NAC d(32), AC s(16)
			465MS		468			ND ob(58), CN t(50), NA t(28), ND:O b(11)
				459MS		459		ND ob(56), CN t(51), NA t(32), ND:O b(12)
							450	CN t(58), ND ob(51), NA t(36), ND:O b(12)
		374MS					372	B b1(27), B b2(17), NAC d(10)
374M			372M		371			B b1(26), CO ib(22), CNA d(13), NAC d(12)
	374MS			372M		370		B b1(28), CO ib(24), CNA d(15)
	326W			326MW		321		B b2(51), ACN d(16)
		308MS					311	CO ib(22), CNA d(21), B b2(21), NAC d(17), ACN d(15)
287W		(289M)[e]	288M		287			B b2(55), B b1(11), CO ib(11)
262MS					259			B b2(20), AB t(16), AC t(13), ACN d(11)
							228	AB t(91)
						228		AB t(84)
					216			AB t(80)
		207M					207	B b2(37), ACN d(14), B b1(12)
	187MS			185MW		195		B b1(17), B b2(15), ACN d(10)
	162M			162MW		171		CNA d(27), AC t(24), ACN d(15)
		161M					159	ND ob(25), NA t(20), CNA d(12), ACN d (10)

Table V   (*Continued from the previous page*)

					α_I-PLA-ND			
		Observed Frequencies[a]				Calculated Frequencies		
	Raman			IR				
A	E_1	E_2	A	E_1	A	E_1	E_2	Potential Energy Distribution[b]
					150			ACN d(24), CNA d(19), NAC d(19), AC t(18), NA t(15)
				115M		125		AC t(23), NA t(21), CN t(18), B b2(10)
120M			122M		118			AC t(24), NA t(17), D:O s(14), CNA d(14), CN t(13)
		86MS		(88VW)[f]			95	CN t(35), AC t(27), CNA d(14)
		60sh					75	AC t(31), NA t(15), B b1(14)
							47	AC t(66), NA t(35), D:O s(29), ND ob(26)
						41		CN t(25), AC t(23), ND ob(18), NA t(12), D:O s(11)

[a] V: very; S: strong; M: medium; W: weak; sh: shoulder.

[b] Diagonal contributions ≥ 10. A: C_α; B: C_β; Ha: H_α; Hb: H_β; CH3: side chain methyl group; H:O: H$\cdots$O (hydrogen bond); s: stretch; b: angle bend; d: deformation; ab: antisymmetric angle bend; r: rock; sb: symmetric angle bend; ob: out-of-plane angle bend; t: torsion.

[c] The unperturbed frequency of this band is predicted near 3314 cm^{-1} due to FR between the NH s fundamental and the first overtone of amine II(A).[44]

[d] FR analysis gives values near 2930 cm^{-1} as the unperturbed frequency of this band.[51,52]

[e] We cannot independently separate E_2-species from A-species modes for a uniaxially oriented sample, and our E_2 spectra contain some bands due to the α_{xx} component (A species).[22] After trials, this band was better assigned to the A species rather than to the E_2 species, and in some cases the observed ir A band clearly supported this assignment.

[f] From the polarized Raman spectra, bands near 84 cm^{-1} are well assignable to E_2 modes, which are not active in the ir. Observation of this ir band with a very weak intensity is possibly due to some irregularities in the helical structure, or to end effects.

[g] The unperturbed frequency of this band is predicted near 2449 cm^{-1} from the FR analysis.[44]

Except for small details, the results shown here are nearly the same as those in a previous study.[48] Since peaks in an inelastic neutron scattering (INS) spectrum of a molecule represent the energy gain or loss of the scattered neutrons by the quanta of molecular rotational or vibrational energy, they are closely related to the density of phonon states of the molecule; especially in the incoherent scattering process, they correspond to the higher density of phonon states. It is well known that in the INS process the hydrogen atom mainly acts as an incoherent scatterer and its incoherent scattering cross section is approximately an order of magnitude larger than those of other nuclei, so that the modes involving the displacements of hydrogen atoms dominate the INS spectrum.[49] Therefore, it is believed that the calculated peak positions in Table VI having large PED contributions from coordinates like $C_\alpha C_\beta$ t, H$\cdots$O s, or NH ob, etc., will give rise to the observed peaks in the INS spectrum of α-PLA.[50] (Different from the selection rules of optically active vibrational transitions, all phase difference values in the first Brillouin zone are permitted in the INS process). Overall, the observed INS peaks are well assignable to the calculated peak points of phonon density. Attention should be paid to the observed strong peak near 230 cm^{-1}, which is well ac-
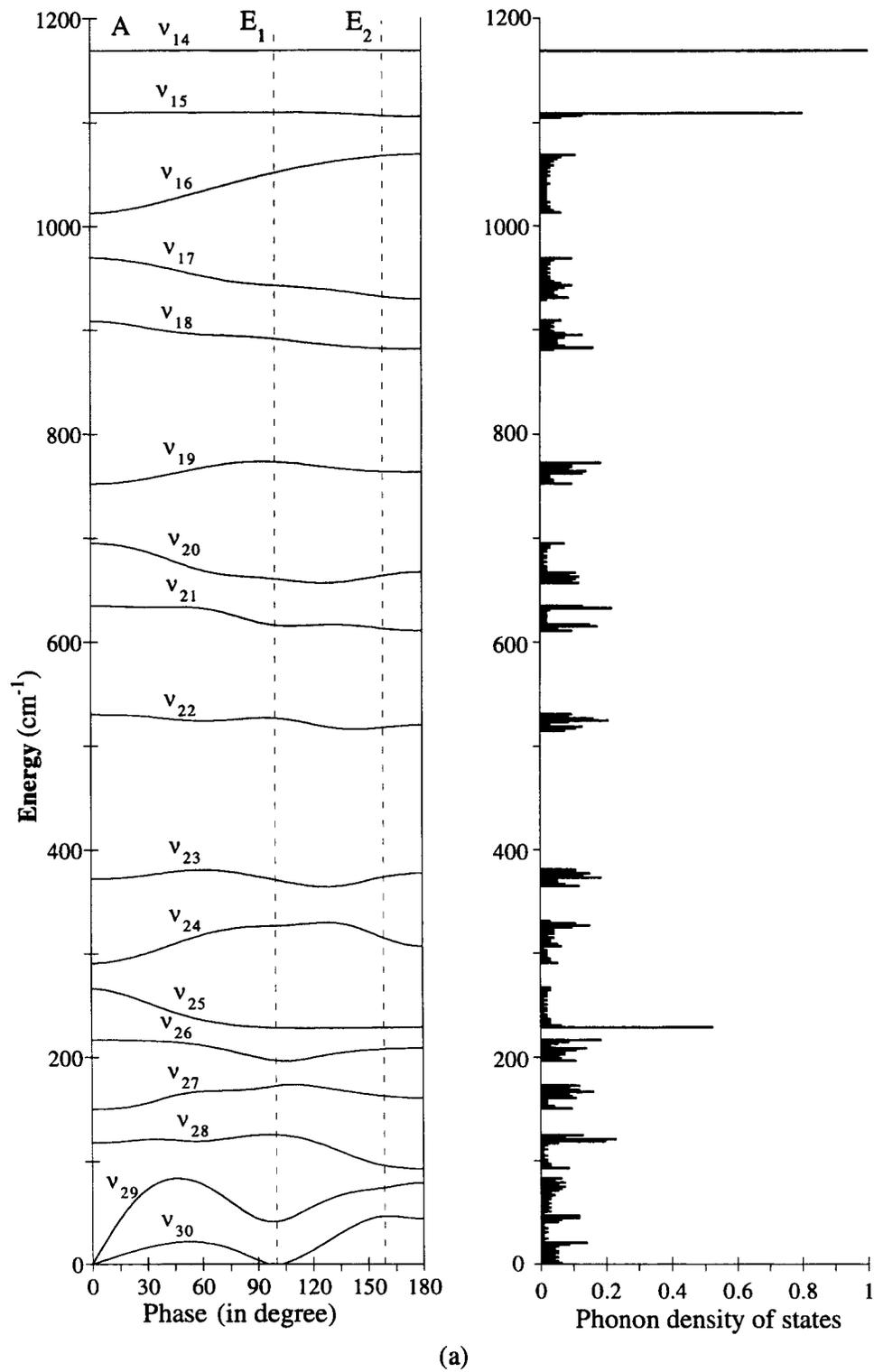
FIGURE 3 Dispersion curves and phonon density of states of α_1-PLA: (a) $0-1200$ cm^{-1} region and (b) $1200-3400$ cm^{-1} region.
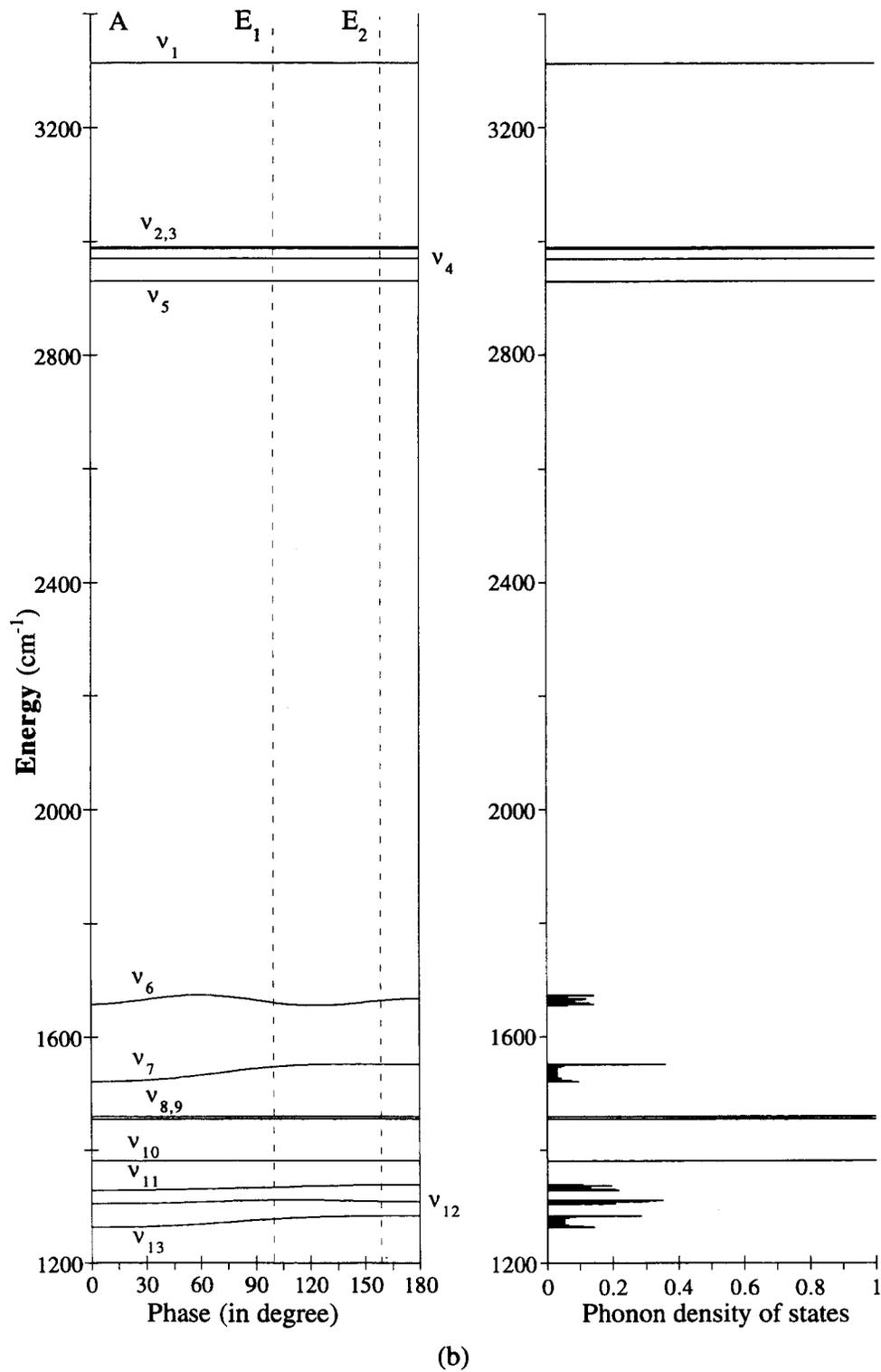
FIGURE 3   (*Continued from the previous page*)

Table VI Calculated Main Peaks in Phonon Density of States and Observed INS Peaks of α-PLA

Obs.[a]	Peak Positions		Potential Energy Distribution[b]
	Calc.	Branch	
	22	ν_{30} (52°) :	NH:O d(27), CN t(20), NA t(18), NH ob(12), AC t(12)
	44	ν_{30} (180°) :	AC t(84), NA t(78), NH ob(28)
	47	ν_{30} (160°) :	AC t(65), NA t(33), H:O s(30), NH ob(25)
	79	ν_{29} (180°) :	AC t(28), B b1(20), NH ob(11), CNA d(11)
80M (±5)	83	ν_{29} (46°) :	H:O s(54), CNA d(12)
	119	ν_{28} (56°) :	AC t(38), NA t(30), CN t(20)
	121	ν_{28} (34°) :	AC t(27), NA t(19), H:O s(18), CN t(16), CNA d(11)
	126	ν_{28} (96°) :	AC t(25), NA t(21), CN t(18)
165M (±12)	161	ν_{27} (180°) :	NH ob(29), NA t(17), ACN d(10), CNA d(10)
	168	ν_{27} (70°) :	CNA d(20), ACN d(19), NAC d(15), AC t(12), H:O s(11)
	173	ν_{27} (110°) :	AC t(26), CNA d(25), NH ob(16), ACN d(11)
	196	ν_{26} (106°) :	B b1(17), B b2(17), ACN d(11)
	209	ν_{26} (180°) :	B b2(38), ACN d(15), B b1(11)
	217	ν_{26} (0°) :	AB t(84)
230S (±19)	228	ν_{25} (116°) :	AB t(87)
	229	ν_{25} (180°) :	AB t(89)
	307	ν_{24} (180°) :	CO ib(24), CNA d(24), NAC d(18), B b2(18), ACN d(14)
	327	ν_{24} (96°) :	B b2(48), ACN d(16)
	364	ν_{23} (128°) :	B b1(28), CO ib(21), CNA d(13)
	372	ν_{23} (0°) :	B b1(28), CO ib(21), CNA d(12), NAC d(11)
	377	ν_{23} (180°) :	B b1(26), B b2(18), NAC d(12)
	520	ν_{22} (180°) :	NAC d(34), AC s(15)
	524	ν_{22} (64°) :	CO ib(24), AC s(19), NAC d(14), ACN d(11)
	527	ν_{22} (94°) :	NAC d(26), CO ib(19), AC s(18)
	611	ν_{21} (180°) :	CN t(57), NA t(32), NH ob(31)
600M (±70) broad	615	ν_{21} (110°) :	CN t(47), NH ob(38), NA t(26), NH:O d(10)
	617	ν_{21} (132°) :	CN t(52), NH ob(37), NA t(30), NH:O d(11)
	634	ν_{21} (38°) :	CN t(53), NH ob(52), NA t(32), NH:O d(12)
	635	ν_{21} (0°) :	NH ob(56), CN t(52), NA t(34), NH:O d(13)
	657	ν_{20} (126°) :	NH ob(15), CO ib(14), AC s(13), NAC d(11), NA t(10)
	667	ν_{20} (180°) :	CO ib(21), AC s(19), NH ob(17)

[a] From Ref. 50.

[b] Diagonal contributions ≥ 10.

counted for by the dominant portion of PED from CH$_3$ t as predicted by peaks at 217, 228, and 229 cm^{-1}.

Band Analysis

Amide A and Amide B Region. A detailed band analysis of this region is given elsewhere.[44] In the region of the amide A mode (essentially NH s), we observed two bands with strong parallel dichroism at 3321VS(A) and 3283S(A) cm^{-1} for an oriented sample containing nearly no residual DCA [Figure 1(a,b)]. This doublet feature in the amide A mode

is also found in our ir spectrum of an unoriented α-PLA sample.[44] This doublet feature in the amide A band of α-PLA was not seen in previous studies, where only a single broad and strong band was observed near 3293 cm^{-1} in a polarized ir spectrum of an oriented sample[1] and near 3307 cm^{-1} in an ir spectrum of an unoriented sample.[8] We find that all these observed features are highly dependent on the amount of residual DCA in the solid α-PLA film.[44] A similar doublet is observed in the polarized Raman spectrum[22] at 3311MS(A) and 3288M(A) cm^{-1}, i.e., with a smaller splitting, and is associated with a thicker sample containing more DCA than the infrared sample. As the DCA amount in an ori-

ented sample increases, the amide A doublet converges to a slightly broad single band centered near $3295VS(A)$ cm^{-1}, thus showing the same features observed in the previous studies.[1,8] Although the 3283S cm^{-1} band in the amide A doublet is coincident with the characteristic β-PLA band,[1] its strong parallel dichroism is opposite to that of an oriented β-PLA structure, and no other strong characteristic β band (e.g., 1632, 1524, and 1222 cm^{-1}) appears in the spectrum. Considering the observed very weak intensity of 1632 ($\perp$) and 1221 ($\parallel$) cm^{-1} in our sample, the relative intensity of the $3283(A)$ cm^{-1} band to that at $3321(A)$ cm^{-1} is too strong to attribute it to β-PLA. We therefore exclude a β-PLA origin for the $3283S(A)$ cm^{-1} band, and discuss its possible origin in greater detail elsewhere.[44]

In the amide B region, a doublet of nearly the same separation as in the amide A region is observed at $3066MW(A)$ and $3028W(A)$ cm^{-1}. The broad $3066MW(A)$ cm^{-1} band, which seems to be composed of more than one band, probably originates from both an overtone of the $1548VS(E_1)$ cm^{-1} band of α_I-PLA and that of the $1539sh(E_1)$ cm^{-1} band of the additional structure. The $3028W(A)$ cm^{-1} band, which was not reported in previous studies, also disappears on N-deuteration and moves upward with weaker intensity as the amount of residual DCA increases in the sample. This is assigned to an overtone of the $1518W(A)$ cm^{-1} band of α_I-PLA, which is the only major band in this region that is in Fermi resonance (FR) with the amide A fundamental at $3321VS$ (A) cm^{-1} according to our calculation of the anharmonic cubic interaction force constants.[44] Thus, from the resolved band intensities the unperturbed A-species frequency of the amide A mode for α_I-PLA is predicted at $3314(A)$ cm^{-1},[44] which is significantly higher than the value of 3279 cm^{-1} predicted in the previous α-PLA study.[8]

On N-deuteration, we observed three ir bands related to ND s vibrations, at $2468S(A)$, $2438sh(A)$, and $2406MS(A)$ cm^{-1}. The shoulder at 2438 cm^{-1} seems to originate from the additional structure. We assume that the $2406MS(A)$ cm^{-1} band is due to the α_I-helix, and can be considered as a combination of the bands at $1429(A)$ and $1000M(A)$ cm^{-1}, and that this band is in FR with the ND s band at $2468S(A)$ cm^{-1}. A similar FR analysis[44] predicts the unperturbed fundamental frequency of the ND s mode for the α_I-helix at $2449(A)$ cm^{-1}.

A quantitative FR analysis for the additional structure could not be done since the corresponding

amide II(A) band and its overtone could not be clearly identified.[44]

CH Stretch Region. Three main bands were observed in the region related to the CH s vibrations. The first band, an ir doublet at $2987M(A)$ and $2981M(E_1)$ cm^{-1}, on N-deuteration at $2989sh(A)$, $2983M(A)$, and $2979M(E_1)$ cm^{-1}, and a broad Raman band near 2989S cm^{-1}, is assigned to the nearly degenerate CH$_3$ as mode as in previous studies.[18] The second band, which is very strong in Raman at $2941VS(A)$ with a shoulder near 2928 cm^{-1} and a medium weak doublet in ir at $2940MW(E_1)$ and $2929MW(E_1)$ cm^{-1}, on N-deuteration the lower frequency component appearing near $2925MW(E_1)$ cm^{-1}, is assigned to CH$_3$ ss. Rabolt et al.[8] reported that the splitting in this band is temperature dependent. In an ir spectrum, they observed a single band at 2930 cm^{-1} at 373 K, which is the same frequency as in β-PLA at room temperature; a doublet at 2939 and 2925 cm^{-1}, with more intensity in the higher frequency component at 300 K; and at 120 K, a doublet with a splitting increased by 3–4 cm^{-1} and with more intensity in the lower frequency component. As suggested by them, this splitting may be due to the presence of CH$_3$···CH$_3$ nonbonded interactions between adjacent chains, which has not been included in the present force field for α-PLA. It is still a puzzle that the band near 2940 cm^{-1} shows a strong A-species characteristic in Raman, different from a small E_1-species characteristic in ir. The third main band, observed in the ir at $2881MW(A, E_1)$ cm^{-1} (on N-deuteration this band significantly decreasing in intensity) and in the Raman near 2882M cm^{-1}, is assigned to a combination of the bands at $1461MS(A)$ (mainly CH$_3$ ab2) and $1454M(E_1)$ cm^{-1} (mainly CH$_3$ ab1), while this band had been assigned to the methyne C$_\alpha$H$_\alpha$ s in the previous studies.[8,18]

In fact, the main features observed in the CH stretch region of α-PLA are nearly the same as those of L-Ala and (L-Ala)$_2$. In detailed vibrational CD and solution-phase Raman studies on L-Ala and its deuterated isotopomers by Nafie and associates,[51–53] it was reported that when the side chain methyl group is replaced by CD$_3$ the three main bands disappear and a new broad band centered near 2970 cm^{-1} appears, which seems to make this band assignable to C$_\alpha$H$_\alpha$ s. We also observed a weak shoulder at the same position in a Raman E_1 spectrum of α-PLA and in an ir E_1 spectrum of α-PLA-ND, and this band is assigned to C$_\alpha$H$_\alpha$ s. Although this is higher than the well-assigned methyne CH s near 2870–2880 cm^{-1} in hydrocarbons,[54] the pres-

ent assignment is supported by ab initio calculations, which place this mode ~ 100 cm^{-1} higher in (L-Ala)$_2$ than in hydrocarbons (N. G. Mirkin and S. Krimm, private communication). Although the CH$_3$ s vibrations are highly localized, it is very difficult to determine their unperturbed harmonic frequencies without full consideration of anharmonic corrections, since these vibrations are also highly anharmonic as is the amide A vibration. It seems that there is an FR between the CH$_3$ ss fundamental and a combination of CH$_3$ ab1 (E_1) and CH$_3$ ab2 (A). Adopting the result of FR analysis on L-Ala by Nafie and associates, we chose 2930(E_1) cm^{-1} as the approximate unperturbed frequency of the CH$_3$ ss mode observed at 2940MW(E_1) cm^{-1}.

As also reported by Rabolt et al.,[8] two weak bands, both with parallel dichroism, are observed in the ir 2800(A) cm^{-1} region, which disappear on N-deuteration. The 2818W(A) cm^{-1} band could arise from a combination of the 1274M(E_1) cm^{-1} band and amide II at 1548VS(E_1) cm^{-1}, or from a combination of the 1305S(A) cm^{-1} band and amide II at 1518W(A) cm^{-1}, while the 2781VW(A) cm^{-1} band could come from a combination of the 1266(A) cm^{-1} band and amide II at 1518W(A) cm^{-1}.

Amide I and Amide II Region. The calculated PEDs for the amide I modes are about CO s(80) and C$_\alpha$CN d(11), with vibrational transition moments being nearly parallel to the helix axis. We observed a very strong infrared band at 1658VS(A) and a Raman band at 1656VS(A) cm^{-1}, which on N-deuteration shift down to 1648VS(A, ir) and 1647VS(A, Raman) cm^{-1} with CO s(86), CN s(11), and C$_\alpha$CN d(10). Related to the perpendicular components, we observed a strong band at 1659S(E_1, ir) cm^{-1}, and on N-deuteration a strong band in the ir and a medium shoulder in the Raman, both at 1658(E_1) cm^{-1}. An additional important feature is the observation of a new Raman band at 1665MW cm^{-1}, which we find can be assigned to an E_2-species mode.[22] The ir shoulder near 1632 cm^{-1}, which is more prominent in E_1 spectra, on N-deuteration shifting to 1627 cm^{-1}, may arise from a small portion of β-PLA, or from the combination bands involving CO ib and CO ob modes.

In the amide II modes, the calculated PEDs show about NH ib(59) and CN s(34), with vibrational transition moments nearly perpendicular to the helix axis. In the polarized ir spectra we observed a very strong band at 1548VS(E_1) cm^{-1} and a weak band at 1518(A) cm^{-1}, while the corresponding Raman intensities are too weak to be recognized. On N-

deuteration, ND ib now contributes to ir and Raman bands in the 1000–940 cm^{-1} region, most of the modes being highly mixed.

Although the ordinary valence-type force field cannot reproduce the observed splittings in the amide I and amide II bands of α-PLA and β-PLA, a TDC perturbation treatment[55,56] was capable of accounting for the then-observed affects.[8,18] In these perturbation treatments, the amide I and amide II transition dipole moments of each peptide group were considered in a weak coupling approximation[20] to be independent of the phase difference between adjacent groups. Although this treatment is successful in reproducing the observed amide I(A) and amide II(E_1) frequencies, it gives a large deviation for the observed amide I(E_2) frequency, which we now find at 1665 cm^{-1} in the polarized Raman spectrum,[22] and the predicted E_1 frequency is significantly lower than the observed value. In our new TDC analysis for α-PLA,[21] we have shown that the weak coupling assumption, viz., that changes in the dipole moment in a group are due solely to changes in the coordinate displacements in that group, is inadequate to reproduce the observed amide I(E_2) frequency. We find that, in addition to the interaction within the reference group (type 0), interactions of type 1 and type 3 are also important for the α-helix. The calculated amide I(E_2) frequency is very sensitive to the value of the interaction force constant $f(\underline{CO\ s}, CO\ s\ 1)$ (interaction distance ≈ 3.2 Å), and even if only this interaction force constant is combined with the previous α-PLA force field,[18] with its value adjusted to the average value of 0.042 mdyn/Å of the eleven scaled ab initio force constants for the various (L-Ala)$_2$ conformers,[23] the calculated E_2 frequency becomes 1661 cm^{-1}, in close agreement with the observed value.

As a simple way to reproduce all the observed amide I and amide II frequencies, some important nonbonded interaction force constants can be introduced directly into the ordinary valence-type force field, avoiding the perturbation treatment. From the listed ab initio peptide force fields,[23] the important nonbonded interaction force constants of type 0 and type 1 could be easily chosen. Those of type 2 or type 3, which are not available from ab initio calculations of present structures, were selected on the basis of interaction force constant values calculated under the weak coupling approximation through a classical dipole–dipole interaction scheme by using the ab initio dipole moment derivatives for NMA.[24] Even though the calculated values of some force constants, such as $f(\underline{NH\ ib}, NH\ ib\ 1)$ (interaction

distance ≈ 2.8 Å) and $f(\underline{\text{NH ib}}, \text{NH ib } 3)$, are very small from both the ab initio and the dipole–dipole interaction scheme, they are not negligible in the force field refinement since the splitting, in this case of the amide II modes, is very sensitive to their values. The hydrogen-bond-related intergroup force constant $f(\underline{\text{H}\cdots\text{O}} \text{ s}, \text{CO s } 3)$ was also found to be important, since it seems to be non-negligible and to be closely related to the amide I frequency, although no calculation has been done for its value. Of course, each optimized intergroup interaction force constant includes the effects from other interactions, such as hydrogen bonding and van der Waals interactions, in addition to that from TDC. As can be seen, all the observed amide I and amide II bands are very well reproduced.

CH Bend and Amide III Region. For the bending vibrations of the side chain CH_3 groups, five bands are expected to be observable from the symmetry, with modes corresponding to CH_3 ab1 and CH_3 ab2 being nearly degenerate. For the $C_\alpha H_\alpha$ b modes, two nondegenerate vibrations are expected to be observable. From the studies on solution-phase L-Ala and its deuterated isotopomers, Nafie and associates[51] assigned a band at $1459MS$ cm^{-1}, which splits into two bands at $1480S$ and $1460M$ cm^{-1} in the solid phase, to the CH_3 ab mode and a band at 1375sh cm^{-1}, which appears as a distinct band at $1373M$ cm^{-1} on $C_\alpha D_\alpha$ substitution, to the CH_3 ss mode, since all these bands disappear on CD_3 substitution. They also concluded that the two CH_3 r modes occur near 1000 and 900 cm^{-1}, while the two bands at $1351S$ and $1301M$ cm^{-1}, which disappear on $C_\alpha D_\alpha$ substitution, are assignable to $C_\alpha H_\alpha$ bends. This can be a general guide to assign the CH bend modes in the observed α-PLA spectra.

Thus, the observed α-PLA doublet at $1461MS(A)$ and $1454M(E_1)$ cm^{-1} in the ir and at $1460MS(A)$, $1456MS(E_1)$, and $1454S(E_2)$ cm^{-1} in the Raman, are assignable to the nearly degenerate CH_3 ab modes. On N-deuteration, interesting new features related to this doublet were observed that were quite uncertain in previous studies. It seems that CN s mixes heavily with CH_3 ab2 in E_1- and E_2-species vibrations. Due to this mixing, the initial ir $1461MW(E_1)$ cm^{-1} band, CH_3 ab2(86), splits into two bands with increased intensity: one at $1472M(E_1)$ cm^{-1}, CH_3 ab2(36) and CN s(27), and the other at $1445S(E_1)$ cm^{-1}, mainly CH_3 ab2(37) and CN s(25). Although these two bands have nearly the same PEDs, the difference in their ir intensities must be due to their different dipole de-

rivative distributions.[57] The ir A-species CH_3 ab2 mode remains nearly unchanged at $1465M(A)$ cm^{-1}. The CH_3 ab1 E_1 mode is not recognizable in the ir, although it is observed at $1457S(E_1)$ cm^{-1} in the Raman, probably due to the presence of the new strong band at $1445S(E_1)$ cm^{-1}. The newly appearing Raman band near $1429(\text{sh-}A, \text{ W -}E_2)$ cm^{-1} was not considered in the early refinement process since its assignment to a symmetry species was uncertain. However, this band was well predicted as an A-species mode during the refinement process, and must be associated with the calculated frequency at $1428(A)$ cm^{-1}, mainly CN s(49) and ND ib(17), thus reasonably qualifying as the amide II$'$ mode (the more prominent intensity in the E_2 than in A spectrum might be due to an α_{xx} component[22]).

The highly localized bands at $1380W(A, \text{ir})$, $1384MS(E_1, \text{ir})$, and $1381MW(A, \text{Raman})$ cm^{-1}, on N-deuteration at $1377MW(A, \text{ir})$, $1382M$ cm^{-1} (E_1, ir), and $1379MW(A, \text{Raman})$ cm^{-1}, and which were also reported to remain unchanged near 1380 cm^{-1} in β-PLA,[58,59] are assigned to the CH_3 ss mode, and are well reproduced in our calculation.

The observed bands at $1330M(A, \text{ir})$, $1331S(A, \text{Raman})$, and $1337M(E_2, \text{Raman})$ cm^{-1} are assigned to H_α ab2 and $C_\alpha C$ s, with the A-species mode being mostly H_α ab2, while the E_2 mode additionally contains a small amount of NH ib. In the observed bands at $1305S(A, \text{ir})$, $1310M(E_1, \text{ir})$, $1306S(A, \text{Raman})$, and $1313\text{sh}(E_1, \text{Raman})$ cm^{-1}, the E_1 band arises from both H_α ab2 and H_α ab1, while the A band arises mainly from H_α ab1.

The bands assigned to the amide III modes in the previous α-PLA studies are observed at $1266W(A)$ and $1274M(E_1)$ cm^{-1} in the ir and at $1264MW(A)$, $1275MW(E_1)$, and $1285MW(E_2)$ cm^{-1} in the Raman, and all the bands are well reproduced in our calculation. The calculated PEDs show that these bands are closely related to H_α ab1 and amide II. On N-deuteration, the bands related to the $C_\alpha H_\alpha$ bends are well separated: the observed bands at $1327M(A, \text{ir})$, $1323M(E_1, \text{ir})$, $1327S(A, \text{Raman})$, and $1324MS(E_2, \text{Raman})$ cm^{-1} are mostly from H_α ab2, and the highly localized bands at $1295(MW\text{-}A, \text{ W -}E_1, \text{ir})$ and $1296M(A, E_1, E_2, \text{Raman})$ cm^{-1} are assigned mainly to H_α ab1.

The observed bands at $1168M(A, \text{ir})$, $1171MS(E_1, \text{ir})$, and $1167MS(A, \text{Raman})$ cm^{-1}, which on N-deuteration appear at $1168MW(A, \text{ir})$, $1179MW(E_1, \text{ir})$, and $1171M(A, \text{Raman})$ cm^{-1}, arise mainly from NC_α s. The quite weak bands at $1012VW(A, \text{ir})$ and $1015W(A, \text{Raman})$ cm^{-1}, on N-deuteration at $1016MW(A, \text{ir})$ cm^{-1} with more

intensity and at $1017VW(A$, Raman$)$ cm^{-1}, arise mainly from $C_\alpha C_\beta$ s (mixed with CH$_3$ r for α-PLA).

Overall, the bands related to the CH$_3$ r modes cannot be well separated since these vibrations are pretty well mixed with skeletal stretches (and with ND ib in N-deuterated samples). The observed bands at $1108W(A$, ir$)$, $1109M(E_1$, ir$)$, $1106S(A$, E_2, Raman$)$, and $1108MS(E_1$, Raman$)$ cm^{-1} arise mainly from CH$_3$ r1 mixed with $C_\alpha C_\beta$ s, on N-deuteration appearing at $1134VW(A$, ir$)$, $1144W(E_1$, ir$)$, $1134M(A$, Raman$)$, and $1142sh(E_1$, Raman$)$ cm^{-1} due to additional mixing with NC$_\alpha$C d. Throughout the refinement process, the $1106S(E_2)$ cm^{-1} band was not considered, but is well reproduced. A band whose origin is still uncertain was observed near 1094 cm^{-1} as a shoulder on the strong Raman band near $1107S$ cm^{-1}; it was more prominent on N-deuteration, though no related band was observed in the ir spectrum. This might be due to a small amount of β structure.[13,19] The observed bands at $1050MS(E_1)$ and $970W(A)$ cm^{-1} in the ir, and at $1070MW(E_2)$, $1051W(E_1)$, $966MW(A)$, $942VW(E_1)$, and $930MW(E_2)$ cm^{-1} in the Raman, which are not seen in polyglycine I while similar bands are present in β-PLA^2, arise mainly from the side chain CH$_3$ r modes. The $1070MW(E_2)$ band arises from CH$_3$ r2 and a small portion of CH$_3$ r1. The bands near $1050(E_1)$ cm^{-1}, which arise from CH$_3$ r2 and $C_\alpha C_\beta$ s, appear at $1061M(E_1$, ir$)$ cm^{-1} and $1062MW(E_1$, Raman$)$ cm^{-1} on N-deuteration. The band at $970W(A$, ir$)$ and $966M(A$, Raman$)$ cm^{-1}, which arises from CH$_3$ r2, C$_\alpha$C s, NC$_\alpha$ s, and $C_\alpha C_\beta$ s, seems to split in α-PLA-ND into two bands—one at $1000M(A$, ir$)$ and $1001MS(A$, Raman$)$ cm^{-1} and the other at $946(MW$, ir, M, Raman$)(A)$ cm^{-1}—due to the interaction with ND ib; and the newly appearing bands at $974W(E_1$, ir$)$, $973M(E_1$, Raman$)$, and $968M(E_2$, Raman$)$ cm^{-1} arise mostly from ND ib and can be assigned to the amide III$'$ modes. The Raman $942VW(E_1)$ cm^{-1} band [which was not considered in the early stages of the refinement process, but when we tried to reproduce the observed bands at $966MW(A)$ and $930MW(E_2)$ cm^{-1} the calculated E_1 frequency quickly converged to the value of this band] appears as a weak shoulder at $936sh(E_1)$ cm^{-1} on N-deuteration, and it is well predicted by the calculated frequency of $931(E_1)$ cm^{-1} with nearly the same PED as that of $942VW(E_1)$ cm^{-1}, viz., mainly from CH$_3$ r2 and NC$_\alpha$ s. The band at $930MW(E_2)$ cm^{-1}, which arises mainly from both CH$_3$ r2, CN s, and NC$_\alpha$ s, appears at $922W(E_2)$ cm^{-1} in α-PLA-ND.

Skeletal Deformation and Other Amide Modes. The three observed bands near the 900 cm^{-1} region, which move down a little on N-deuteration, are well reproduced in our calculation and arise from CNC$_\alpha$ d, CO ib, CH$_3$ r1, and $C_\alpha C_\beta$ s: the band at $908(M$, ir, VVS, Raman$)(A)$ cm^{-1}, on N-deuteration at $887M(A$, ir$)$ and $888VVS(A$, Raman$)$ cm^{-1}, arises mainly from CNC$_\alpha$ d and CO ib; the band at $891M(E_1$, ir$)$ and $892sh(E_1$, Raman$)$ cm^{-1}, on N-deuteration at $882M(E_1$, ir$)$ cm^{-1}, comes from $C_\alpha C_\beta$ s, CH$_3$ r1, and CO ib; while the Raman band at $882MW(E_2)$ cm^{-1}, on N-deuteration at $878sh(E_2)$ cm^{-1}, contains a dominant $C_\alpha C_\beta$ s component. The ND-Raman band at $878sh(E_2)$ cm^{-1} was not considered in the early stages of refinement, but it was well predicted as a result of the fitting process for the other bands. Note that the origin of very strong Raman intensity in the A-species band at 908 cm^{-1}, at 888 cm^{-1} on N-deuteration, was considered to be due mostly to CN s(23), CNC$_\alpha$ d(16), and CO ib(12) in the previous analysis,[18] while our new result attributes it mainly to CNC$_\alpha$ d and CO ib, with a small CN s(8) contribution.

The observed bands at $772MW(E_1)$ cm^{-1} in the ir and at $752MW(A)$ and $753MW(E_2)$ cm^{-1} in the Raman, on N-deuteration at $764M(E_1$, ir$)$, $751W(A$, Raman$)$, and $753MW(E_2$, Raman$)$ cm^{-1}, arise mainly from the CO ob mode, whose transition moment is nearly perpendicular to the helix axis and is expected to remain nearly unchanged on N-deuteration, and these bands can be assigned to the amide VI modes. A poorly resolved weak broad band centered near 773 cm^{-1} was observed in all Raman spectra; it is more prominent in E_1 spectra and moves down near 764 cm^{-1} on N-deuteration. The observed Raman $753MW(E_2)$ cm^{-1} band seems to arise from the α_{xx} component,[22] and after trials was not considered in the refinement process.

Incidentally, we noticed that the frequencies in this region are significantly affected by the hydrogen-bonded angle-bend force constants. The only available ab initio hydrogen-bond force constants were those calculated by Cheam using the 3-21G basis set on a model complex of NMA hydrogen bonded at the NH and CO groups to two formamide molecules.[24] At the early stage of the refinement process, when we tried to use the ab initio hydrogen-bonded angle-bend force constants, $f(\text{NH}\cdots\text{O b}) = 0.11$ mdynÅ and $f(\text{CO}\cdots\text{H b}) = 0.05$ mdynÅ, which were scaled by a scale factor 0.86, the calculated frequency of NH$\cdots$O b was higher than that of CO ob, while the frequency of ND$\cdots$O b was lower than that of CO ob. No observed band could

be found corresponding to this predicted frequency behavior of NH···O b, and in order to reproduce the observed amide VI modes and other lower frequency modes we had to reduce these force constant values to $f(NH···O$ b$) = 0.0147$ mdynÅ and $f(CO···H$ b$) = 0.010$ mdyn/Å. Our refined force constant value of the hydrogen-bonded H···O s, 0.141 mdyn/Å, is also smaller than the corresponding ab initio value, 0.24 mdyn Å, which was scaled by a scale factor 0.80. What this says is that even though the (scaled) ab initio force constants are reliable, the force constants related to the hydrogen-bonded coordinates still need to be further improved.

The three observed bands at 693MW(A) and 659MS(E_1) cm^{-1} in the ir and at 693MW(A, E_2) and 661MW(E_2) cm^{-1} in the Raman, which on N-deuteration slightly move down to 682MW(A, ir), 649M(E_1, ir), 685(W-A, M-E_2, Raman), and 655M(E_2, Raman) cm^{-1}, showing a similar behavior between A and E_1 modes, arise from skeletal deformation and C_αC s. Our well-reproduced calculation shows that the A band arises mainly from NC$_\alpha$C d and the corresponding E_2 species arises mainly from CO ib and C$_\alpha$C s. Our assignment of the band near 660(E_1) cm^{-1} to skeletal deformation and small portions of NH ob, NC$_\alpha$ t, and CN t is totally different from that of the previous α-PLA studies, in which it was improperly assigned to CN t and NH ob and considered as one of the amide V modes. Even though the Raman band near 693 cm^{-1} shows more intensity in E_2 than in A spectra, it is better assigned to the A species from the observed ir band at 693MW(A) cm^{-1}, the observed Raman intensity in the E_2 spectra arising from an α_{xx} component.[22]

The observed slightly broad ir bands at 639M(A) and 612MS(E_1) cm^{-1} and a broad Raman band centered near 638MW(A) cm^{-1} disappear on N-deuteration, and possibly related to these bands, two very broad bands newly appear near 465MS(A) and 459MS(E_1) cm^{-1} in the ir. The bands at 612MS(E_1, ir) and 459MS(E_1, ir) cm^{-1} are confidently assignable to NH ob and ND ob, respectively, whose transition moments are nearly perpendicular to the helix axis. The observed ir ND band at 465MS(A) cm^{-1} was not considered in the early stages of the refinement process, but during the reproduction of other observed bands it was fairly well predicted and it was considered near the final stages with a smaller weight factor than other bands. Our well-reproduced calculations reasonably account for the observed band intensities at 465MS(A) cm^{-1}, as

well as at 639M(A) cm^{-1}. The observed ir NH bands at 639M(A) and 612MS(E_1) cm^{-1} can be assigned to the amide V modes, while the observed ND bands near 465MS(A) and 459MS(E_1) cm^{-1} can be assigned to the amide V ′ modes. The calculation shows a nearly equal mixing between NH ob (ND ob) and CN t in the amide V (V ′) modes. The amide V (V ′) modes can give significant peaks in INS spectra and our calculation also well accounts for the observed INS band near 600M ($\pm$70) cm^{-1} (Table VI). The weak bands at 623W(A) and 593VW(E_1) cm^{-1}, shown in far-ir ND spectra, seem to arise from a small portion of β structure in this oriented sample[58,59] [this thicker sample may have more β structure than the thinner samples used for the ir spectra of Figure 1 (a)–(h)].

The observed bands near 529 cm^{-1}, on N-deuteration near 524 cm^{-1}, which are fairly strong in both the ir (A, E_1) and the Raman (A, E_1, E_2) with slightly higher intensity in the A species, are assigned to the amide IV (IV ′) modes, as in the previous α-PLA studies.[8,18] Our well-reproduced calculation shows that the A-species bands are mainly due to CO ib mixed with C$_\alpha$C s and C$_\alpha$CN d, while the E_1 and E_2 species arise from NC$_\alpha$C d mixed with C$_\alpha$C s and CO ib. In the refinement process the E_2 bands were not considered and the E_1 bands were given smaller weight factors than the A bands.

Low Frequency Region. The observed bands at 374M(A) and 373M(E_1) cm^{-1} in the ir and at 375M(A) and 374(M-E_1, MS-E_2) cm^{-1} in the Raman, on N-deuteration at 372M(A, E_1, ir) and 374(M-A, MS-E_1, MS-E_2, Raman) cm^{-1}, are well reproduced by our calculation. The slightly more intense Raman E_2 bands arise from C$_\beta$ b1 mixed with C$_\beta$ b2, while the A and E_1 bands are due to both C$_\beta$ b1 and CO ib mixed with CNC$_\alpha$ d. The observed bands at 289M(A, ir), 328MW(E_1, ir), and 329W(E_1, Raman) cm^{-1}, on N-deuteration at 288M(A, ir), 326MW(E_1, ir), and 326W(E_1, Raman) cm^{-1}, arise mainly from C$_\beta$ b2, and the Raman E_2 band at 311M cm^{-1}, on N-deuteration at 308MS cm^{-1}, arises from skeletal deformations mixed with C$_\beta$ b2. The observed Raman band at 290MW(E_2) cm^{-1}, on N-deuteration at 289M(E_2) cm^{-1}, seems to arise from the α_{xx} component (A species).[22] If we assume the 290MW(E_2) cm^{-1} band as a real E_2-species mode, we have to assign not only this band but also the ir 289M(A) cm^{-1} band to fairly localized C$_\alpha$C$_\beta$ t modes, whose vibrational intensity is believed to be very weak in Raman and ir spec-

tra,[60] and this assumption is highly unlikely in view of both the observed vibrational intensities and the observed strong INS peak[50] near 230S (± 19) cm^{-1} related to C$_\alpha$C$_\beta$ t.

The observed broad and very weak band at 242VW(E_1, ir) cm^{-1}, on N-deuteration at 251VW(E_1, ir) cm^{-1}, was not considered in the refinement process, although it was assigned to C$_\alpha$C$_\beta$ t in the previous α-PLA studies.[8,18] Our new analysis shows that the observed bands at 263(VW, ir, MS, Raman)(A), on N-deuteration at 262MS(A, Raman), is mainly due to C$_\beta$ b2 mixed with C$_\alpha$C t and C$_\alpha$C$_\beta$ t. Considering the significant Raman intensity in this band, and in order to give a pretty localized PED in the A-species C$_\alpha$C$_\beta$ t vibration, f(C$_\alpha$C$_\beta$ t) was decreased to 0.094 mdyn from the previous value of 0.110 mdyn.[18] As mentioned previously, our calculation also well accounts for the observed INS peak near 230S (± 19) cm^{-1} related to C$_\alpha$C$_\beta$ t (Table VI). The observed Raman E_2 band at 209M cm^{-1}, on N-deuteration at 207M cm^{-1}, is well reproduced and arises mainly from C$_\beta$ b2 and C$_\alpha$ CN d.

The observed bands at 188MW(E_1) cm^{-1} in the ir and at 189M(E_1) cm^{-1} in the Raman, on N-deuteration at 185MW(E_1, ir) and 187MS(E_1, Raman) cm^{-1}, may arise from C$_\beta$ b1 and C$_\beta$ b2, while the observed bands at 163(MW, ir, M, Raman) (E_1) cm^{-1}, on N-deuteration at 162(MW, ir, M, Raman) (E_1) cm^{-1}, are mainly due to CNC$_\alpha$ d and C$_\alpha$C t. The observed Raman E_2 band at 162M cm^{-1}, on N-deuteration at 161M cm^{-1}, which has nearly the same intensity and frequency as those of the E_1 band, is considered to be a real E_2 band in view of the observed weak intensity in the A spectra,[22] and may arise from NH ob (ND ob) and NC$_\alpha$ t. The observed weak shoulder near 157sh(E_2) cm^{-1} in the Raman, which is more prominent on N-deuteration, may arise from combinations of the calculated frequencies at 125(E_1) and 41(E_1) cm^{-1}, both in NH and ND spectra.

The observed bands at 119M(A) and 116M(E_1) cm^{-1} in the ir and at 119sh(A) and 84M(E_2) cm^{-1} in the Raman, on N-deuteration at 122M(A, ir), 115M(E_1, ir), 120M(A, Raman), and 86MS(E_2, Raman) cm^{-1}, arise mainly from backbone torsions. Note that the correct band assignment in these well-separated bands is crucial to estimate the correct values of backbone torsion force constants. In order to reproduce the observed frequency values near 120 cm^{-1} in A and E_1 spectra, which arise mainly from C$_\alpha$C t and NC$_\alpha$ t, the values of f(C$_\alpha$C t) and f(NC$_\alpha$ t) have to be significantly increased from the previous small values[18] of 0.06 and 0.087 mdyn, respectively, and this indeed is also consistent with

the ab initio results for various (L-Ala)$_2$ conformers. The hydrogen-bonded H···O s (D···O s) vibration appears as a small component in the A-species mode. The observation of a very weak ir band at 84VW(E_1) cm^{-1}, on N-deuteration at 86VW(E_1) cm^{-1}, where only Raman active E_2 modes are well assigned, may be due to some irregularities in the helical structure or to end effects. Below the 70 cm^{-1} region, there were no reliable experimental results available. Our calculation shows that all modes in this region are mainly due to backbone torsions, in some cases mixed with hydrogen-bonded H···O s (D···O s).

CONCLUSIONS

New experimental and theoretical studies have led to significant improvements in our understanding of the vibrational dynamics of α-helical poly-(L-alanine). Our definitive polarized Raman (A, E_1, E_2) and ir (A, E_1) spectra for oriented samples of α-PLA and its N-deuterated analogue have permitted more accurate band assignments than were previously possible. All the assigned bands are very well reproduced (to less than 5 cm^{-1} above 200 cm^{-1}) as a result of a least-squares refinement process based on the ab initio force fields of small peptides like NMA and (L-Ala)$_2$. The resulting refined force field also well explains the observed INS spectra of α-PLA samples,[50] thus providing a solid base for the vibrational analysis of other helical polypeptides as well as supporting the reliability of the force field.

Another new feature of our force field is the introduction of direct nonbonded interaction force constants to reproduce observed splittings between symmetry species for amide I and amide II modes. This not only gives a more accurate and simple TDC description of these splittings, but it avoids the weak coupling and perturbation assumptions of previous treatments. The analysis of the ab initio peptide force fields shows that, besides structure-independent force constants that can be moderately transferable to other peptide structures, there are structure-sensitive interaction force constants that cannot be directly transferable and whose conformation dependence should be determined in order to obtain comparably accurate normal mode analyses. Overall, we find that ab initio quantum mechanical calculations for small peptides provide reasonable interaction force constants for polypeptides, although the hydrogen-bonded force constants are

somewhat overestimated and need to be further improved.

REFERENCES

1. Elliott, A. (1954) *Proc. Roy. Soc. London* **A226,** 408–421.
2. Bamford, C. H., Elliott, A. & Hanby, W. E. (1956) *Synthetic Polypeptides,* Academic Press, New York.
3. Miyazawa, T., Fukushima, K., Sugano, S. & Masuda, Y. (1967) in *Conformation of Biopolymers,* Vol. II, Ramachandran, G. N., Ed., Academic Press, New York, pp. 557–568.
4. Itoh, K., Nakahara, T., Shimanouchi, T., Oya, M., Uno, K. & Iwakura, Y. (1968) *Biopolymers* **6,** 1759–1766.
5. Itoh, K., Shimanouchi, T. & Oya, M. (1969) *Biopolymers* **7,** 649–658.
6. Masuda, Y., Fukushima, K., Fujii, T. & Miyazawa, T. (1969) *Biopolymers* **8,** 91–99.
7. Itoh, K. & Shimanouchi, T. (1970) *Biopolymers* **9,** 383–399.
8. Rabolt, J. F., Moore, W. H. & Krimm, S. (1977) *Macromolecules* **10,** 1065–1074.
9. Koenig, J. L. & Sutton, P. L. (1969) *Biopolymers* **8,** 167–171.
10. Fanconi, B., Tomlinson, B., Nafie, L. A., Small, W. & Peticolas, W. L. (1969) *J. Chem. Phys.* **51,** 3993–4005.
11. Simons, L., Bergström, G., Blomfelt, G., Forss, S., Stenbäck, H. & Wansén, G. (1972) *Commentat. Phys.-Math., Soc. Sci. Fenn.* **42,** 125–207.
12. Fanconi, B. (1973) *Biopolymers* **12,** 2759–2776.
13. Frushour, B. G. & Koenig, J. L. (1974) *Biopolymers* **13,** 455–475.
14. Chen, M. C. & Lord, R. C. (1974) *J. Am. Chem. Soc.* **96,** 4750–4752.
15. Tipping, M., Viras, K. & King, T. A. (1984) *Biopolymers* **23,** 2891–2899.
16. Krishnan, M. V. & Gupta, V. D. (1970) *Chem. Phys. Lett.* **6,** 231–234.
17. Fanconi, B., Small, E. W. & Peticolas, W. L. (1971) *Biopolymers* **10,** 1277–1298.
18. Dwivedi, A. M. & Krimm, S. (1984) *Biopolymers* **23,** 923–943.
19. Krimm, S. & Bandekar, J. (1986) *Adv. Protein Chem.* **38,** 181–364.
20. Higgs, P. W. (1953) *Proc. Roy. Soc. London* **A133,** 472–485.
21. Lee, S.-H. & Krimm, S. *Chem. Phys.,* in press.
22. Lee, S.-H. & Krimm, S. (1998) *J. Raman Spectrosc.* **29,** 73–80.
23. Lee, S.-H. (1997) *Ph.D. thesis,* University of Michigan, Ann Arbor.
24. Cheam, T. C. (1992) *J. Mol. Struct. (Theochem.)* **257,** 57–73.
25. Mirkin, N. G. & Krimm, S. (1991) *J. Mol. Struct.* **242,** 143–160.
26. Cheam, T. C. & Krimm, S. (1989) *J. Mol. Struct. (Theochem.)* **188,** 15–43.
27. Cheam, T. C. & Krimm, S. (1990) *J. Mol. Struct. (Theochem.)* **206,** 173–203.
28. Cheam, T. C. (1993) *J. Mol. Struct.* **295,** 259–271.
29. Fletcher, R. & Reeves, C. M. (1963) *Comput. J.* **6,** 163–168.
30. Polak, E. (1971) *Computational Methods in Optimization: A Unified Approach,* Academic Press, New York.
31. Levenberg, K. (1944) *Quart. Appl. Math.* **2,** 164–168.
32. Marquardt, D. W. (1963) *J. Soc. Ind. Appl. Math.* **11,** 431–441.
33. Brown, L. & Trotter, I. F. (1956) *Trans. Farad. Soc.* **52,** 537–548.
34. Shimanouchi, T. & Mizushima, S. (1955) *J. Chem. Phys.* **23,** 707–711.
35. Miyazawa, T. (1961) *J. Polymer Sci.* **55,** 215–231.
36. Sugeta, H. & Miyazawa, T. (1967) *Biopolymers* **5,** 673–679.
37. Arnott, S. & Dover, S. D. (1967) *J. Mol. Biol.* **30,** 209–212.
38. Pauling, L. & Corey, R. B. (1951) *Proc. Nat. Acad. Sci. USA* **37,** 235–240.
39. Leach, S. J., Némethy, G. & Scheraga, H. A. (1966) *Biopolymers* **4,** 887–904.
40. Némethy, G., Phillips, D. C., Leach, S. J. & Scheraga, H. A. (1967) *Nature* **214,** 363–365.
41. Ramachandran, G. N. & Sasisekharan, V. (1968) *Adv. Protein Chem.* **23,** 283–438.
42. Cantor, C. R. & Schimmel, P. R. (1980) *Biophysical Chemistry,* Part I, Freeman, San Francisco.
43. Barlow, D. J. & Thornton, J. M. (1988) *J. Mol. Biol.* **201,** 601–619.
44. Lee, S.-H., Mirkin, N. G. & Krimm, S., to be published.
45. Pavone, V., Di Blasio, B., Santini, A., Benedetti, E., Pedone, C., Toniolo, C. & Crisma, M. (1990) *J. Mol. Biol.* **214,** 633–635.
46. Wilson, E. B., Decius, J. C. & Cross, P. C. (1955) *Molecular Vibrations,* McGraw-Hill, New York.
47. Abe, Y. & Krimm, S. (1972) *Biopolymers* **11,** 1817–1839.
48. Datye, V. K. & Krimm, S. (1986) *J. Chem. Phys.* **84,** 6989–6996.
49. Trevino, S. F. (1968) *Appl. Spectrosc.* **22,** 659–674.
50. Drexel, W. & Peticolas, W. L. (1975) *Biopolymers* **14,** 715–721.
51. Diem, M., Polavarapu, P. L., Oboodi, M. & Nafie, L. A. (1982) *J. Am. Chem. Soc.* **104,** 3329–3336.
52. Lal, B. B., Diem, M., Polavarapu, P. L., Oboodi, M.,

Freedman, T. B. & Nafie, L. A. (1982) *J. Am. Chem. Soc.* **104,** 3336–3342.

53. Oboodi, M. R., Alva, C. & Diem, M. (1984) *J. Phys. Chem.* **88,** 501–505.
54. Mirkin, N. G. & Krimm, S., to be published.
55. Krimm, S. & Abe, Y. (1972) *Proc. Natl. Acad. Sci. USA* **69,** 2788–2792.
56. Moore, W. H. & Krimm, S. (1975) *Proc. Natl. Acad. Sci. USA* **72,** 4933–4935.
57. Qian, W. & Krimm, S. (1993) *J. Phys. Chem.* **97,** 11578–11579.
58. Dwivedi, A. M. & Krimm, S. (1982) *Macromolecules* **15,** 186–193.
59. Dwivedi, A. M. & Krimm, S. (1983) *Macromolecules* **16,** 340.
60. Durig, J. R., Caraven, S. M. & Harris, W. C. (1972) in *Vibrational Spectra and Structure,* Vol. 1, Durig, J. R., Ed., Marcel Dekker, New York, pp. 73–177.